VILNIUS UNIVERSITY

CENTER FOR PHYSICAL SCIENCES AND TECHNOLOGY

Monika

SKRUODIENĖ

Synthesis and Investigation of Terbium and Chromium Co-doped Yttrium Aluminum Garnet

DOCTORAL DISSERTATION

Life Sciences,

Chemistry N 003

VILNIUS 2019

This dissertation was written between 2014 and 2018 at Vilnius University.

Academic supervisor:

Assoc. Prof. Dr. Artūras Katelnikovas (Vilnius University, Life sciences, Chemistry, N 003); From 1/10/14 to 3/9/15.
Assoc. Prof. Dr. Ramūnas Skaudžius (Vilnius University, Life sciences, Chemistry, N 003); From 4/9/15 to 30/9/18.

VILNIAUS UNIVERSITETAS

FIZINIŲ IR TECHNOLOGIJOS MOKSLŲ CENTRAS

Monika

SKRUODIENĖ

Itrio aliuminio granato, legiruoto terbiu ir chromu, sintezė ir tyrimas

DAKTARO DISERTACIJA

Gamtos mokslai,

Chemija N 003

VILNIUS 2019

Disertacija rengta 2014– 2018 metais Vilniaus universitete.

Mokslinis vadovas:
doc. dr. Artūras Katelnikovas (Vilniaus universitetas, gamtos mokslai, chemija – N 003). Nuo 2014-10-01 iki 2015-09-03.
doc. dr. Ramūnas Skaudžius (Vilniaus universitetas, gamtos mokslai, chemija – N 003). Nuo 2015-09-04 iki 2018-09-30.

CONTENTS

LIST OF ABBREVIATIONS

CCD	Charge-coupled device
CRT	Cathode-ray tubes
DTA	Differential Thermal Analysis
DTG	Derivative thermogravimetry
EQE	External quantum efficiency
GSGG	Gadolinium scandium gallium garnet
IPCE	Incident photon to converted electron
IQE	Internal quantum efficiency
LD	Laser diode
LED	Light emitting diode
LNTh	Luminescent nano-thermometer
PTA	Photo-thermal ablation
QE	Quantum efficiency
RE	Rare-Earth
SEM	Scanning electron microscopy
TGA	Thermogravimetric analysis
TAG	Terbium aluminum garnet
UC	Up-conversion
wLED	White light emitting diode
XRD	X-ray diffraction
YAG ($Y_3Al_5O_{12}$)	Yttrium aluminum garnet
YAM	Yttrium aluminum monoclinic
YAP	Yttrium aluminum perovskite

INTRODUCTION

Nowadays, the majority of optical and optoelectronic devices, including light emitting diodes, generators, detectors, transmitters, splitters, etc., have been successfully created. Currently, research and development are focused on novel applications of these devices and their implementation as structural elements in fully integrated systems. Hence, new techniques with novel advanced materials need to be developed for the fabrication of such systems [1, 2].

As a matter of fact, compact light sources are required for plenteous fields, such as sensing applications, spectroscopy or analytical techniques. Recently, solid-state lasers devices have attracted amplified attention, and every day, new ones are created. For this reason, the need to improve the characteristics and properties of the high-power laser through the downsizing of the active material was particularly investigated. Obviously, the optical properties of the active medium are the most crucial issues to overcome, but chemical, thermal or mechanical parameters should be mentioned as well and can be really critical for certain specific applications. Also, the spectroscopic properties of the utilized material have to be deeply considered. In this context, rare-earth-doped materials are one of the most successful classes of active media for solid-state optical devices, including advanced lasers and/or light emitting diode (LED) devices [1-5].

In fact, LEDs are used for applications far beyond lighting. Since the old pocket calculators, where LEDs were employed as red dots for digital numbers, a long way had been since then traveled. In fact, presently, deep-UV LEDs may feed, among others, novel complexes water-quality monitoring networks, micro-LEDs open the doors for optogenetics and near UV LEDs cure adhesives and inks. The latter class can deliver wide extent output for various functions ranging from sensing and adhesive curing to phototherapy [6-9].

More effective LEDs emitting in the near UV are very much substituting lamps for curing various organic inks and/or adhesives. LEDs can operate over 40,000 hours, compared to 1000 – 8000 hours for conventional lamps (mercury based) while dissipating much less electrical energy, decreasing thereby the operating costs. Usually, to take advantage of photo-initiators initially established for mercury lamps, adhesives are cured by UV LED emitting at 365 nm. The deep penetration of the UV wavelength triggers a full-

depth curing process. The ability of LEDs to concentrate optical signal onto tiny regions and small surfaces is also a huge advantage for electronics industries. This is due to their faculty to eliminate light wide spreading that could damage sensitive products, and hence, improving the production yields of particular components, such as touch-screen panels, etc. Moreover, since the recent development of special ink, current printers take also an advantage of the 395 nm UV light for curing it due to the higher LED powers available at that wavelength. In addition, this high power -available usually from 365 to 395 nm – rends the near UV LEDs at those wavelengths very attractive for exciting fluorescence spectroscopy in a wide range of materials. Finally, phototherapy based on near-UV LEDs is also very much promising for destroying pathogens in blood, used for transfusion [9-12].

On the other hand, the concept of a white light emitting diode (wLED) has been sound bizarre until the recent successful establishment of blue/ultraviolet LEDs (2014' Nobel Prize of Physics) [13], when the white LED made its debut. However, generating white light by means of near-UV LEDs not only necessitates the development of new phosphors materials, and also the modification of certain existing ones.

The initial white LED based on phosphors commercially ready for use was fabricated by the Japanese company Nichia Co., which was the first to manage to make the blue LED [14]. To do so, Nichia first created a blue light emitting gallium indium nitride (GaInN) and then coated the chip with yellow fluorescent phosphor cerium doped yttrium aluminum garnet ($Y_3Al_5O_{12}$:Ce, well known now as YAG:Ce). A little bit later, another huge company Osram started to use another matrix – cerium(III) doped terbium aluminum garnet ions (TAG:Ce) [15].

Indeed, YAG is one of the very first synthetic crystalline material of the garnet group, being of a huge interest both for fundamental research and industrial applications. Due to its good thermal conductivity, single crystal garnets are greatly employed in various technological applications, including fluorescent screen, scintillators and solid-state lighting [16-22].

Later on, another yellow phosphor, namely TAG:Ce was also used with GaInN chip for white light manufacturing. YAG and TAG activated with trivalent cerium, have been found to be powerful phosphors for transforming the blue emission-LED into a very broad yellow radiation [14, 23]. In fact, the yellow radiation from YAG:Ce and TAG:Ce are sufficiently intense to

balance the residual blue light which outbreaks over the phosphor in order to produce white light.

Some critical characteristics of garnets include radiation detection, hardness, thermal conductivity, lasing, and magneto-optical behavior. All these unique properties of garnet-based structures will certainly boost the demand for new generation of garnet crystals [23-28]. In addition, as the YAG has a cubic garnet structure and a stable lattice, it is suitable for being a host for phosphors. In fact, during the last two decades, various novel efficient phosphors were successfully synthesized. Inorganic phosphors are made of an inert host lattice and an activator that is optically excited, for example, 3*d* or/and 4*f* electron metal ions, such as Ce^{3+}, Cr^{3+}, Eu^{3+}, Tb^{3+} [17, 28-31]. Co-doped YAG phosphors are largely employed in optical based technologies, phosphors for lasers, luminescent and telecommunication systems based on optical fiber for medical treatment [21, 32-35].

Among the rare-earth materials, terbium is identified to be one of the most significance. It offers a high catalytic behavior and is employed in various applications, including light emission treatment for which it has demonstrated an unprecedented potential [36]. Such characteristics rend the terbium seriously in demand for advanced materials and applications.

Thus, the main aim of this doctoral thesis is synthesis and investigation of optical properties of terbium and/or chromium (co-)substituted yttrium aluminum garnets. In order to achieve these aims the following tasks were set:

- To synthesize terbium and/or chromium ions (co-)substituted yttrium aluminum garnet using sol-gel processing route.
- To investigate the effect of the concentration influence of Tb^{3+} ions of YAG:1%Cr^{3+} on the luminescence properties and kinetics.
- To find the optimal concentration of Cr^{3+} with respect to the highest emission value.
- To compare the external quantum efficiency of YAG:x%Tb^{3+} and YAG:1%Cr^{3+}, x%Tb^{3+}.

1. OBSERVATION OF LITERATURE

1.1. Structure and synthesis of garnets

1.1.1. Structure of garnets

From an etymological point of view, the word “garnet” originates from the fourteenth-century Middle English word “gernet” which means “dark red”. The latter is in turns derivatives from the Latin “granatus”, or “granum” (meaning literally “grain, seed”). This is likely a source to the words “mela granatum” and “pomum granatum” [37]. As a matter of fact, “punica granatum”, which is a plant producing fruits those contain ample and intense red seed covers (arils), which are similar in size, shape, and color to some chemical garnet crystals.

Moreover, natural garnet is not a single material or mineral, but rather refers to a group, containing elements that are closely related in shape. These garnet elements form intermediary minerals between each other and could even intergrow within the same single crystal. The garnets change only somewhat little in their physical characteristics, and often, some of the constituting elements could be so similar that they are almost indistinguishable from one to another without an accurate XRD analysis.

A group of silicate minerals employed as gemstones and abrasives tool since the Bronze Age [38]. In 1928, the crystal structure of the garnet was initially discovered and identified by Menzer [39]. The chemical bonds are gathered into primary and secondary bonding according to the bond strength level. Primary bonds, such as covalent and/or ionic links, have bond energies ranging from 100 to 1000 kJ mol^{-1} [40]. In the YAG structure, this ionic bonding of the oppositely charged ions is occurred by the transfer of electrons between Y^{3+}, Al^{3+}, and O^{2-} ions [41], leading thereby to a very stable crystal arrangement.

Yttrium(III) has a similar ionic radius and chemical properties and can be easily replaced with lanthanide ions such as Eu^{3+}, Nd^{3+}, Tm^{3+}, Er^{3+}, Ce^{3+} or Tb^{3+} in its crystal lattice, making it optically active material (phosphor). Aluminum(III) has a similar ionic radius and can be replaced with 3*d* metal ions, for example, Sc^{3+}, Ti^{3+}, Cr^{3+}, and etc. [44-47].

Garnets have a cubic structure, corresponding to the space group $Ia\bar{3}d$ (#230). The crystal structure of yttrium aluminum garnet is sketched in Fig. 1.

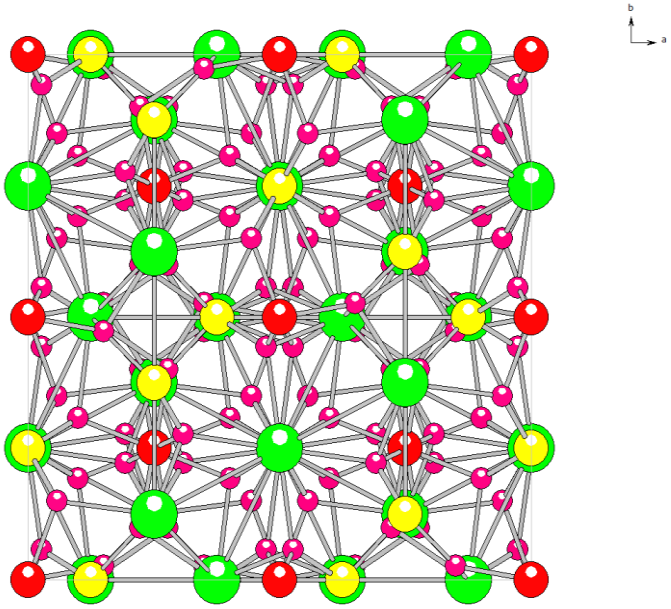

Fig. 1. The crystal structure of YAG. Large yellow circles illustrate aluminum in a tetrahedral site, red circles – aluminum in an octahedral site, green circles – yttrium and purple circles – oxygen (adapted from [42]).

The general garnet compound obeys to the formula $A_3B_2'B_3''O_{12}$, where A, B' and B'' are metal ions in different symmetry sites. The crystal structure of YAG has a bcc structure with 160 atoms in the primitive cell. Each A ion (yttrium ion) is holding 24(*c*) sites and is dodecahedrally coordinated to eight oxygen ions. Meanwhile, oxygen atoms are in 96(*h*) sites and its location is dependent on three structural parameters *x*, *y* and *z* and are different for different garnet oxides. Aluminum ions B' and B'' are occupying two different sites. B' occupies the 16(*a*) (an octahedral) site, and B`` occupies the 24(*d*) (a tetrahedral) site. The formula unit of garnet can be viewed as two octahedrons, three tetrahedrons and three dodecahedrons coordinated with shared oxygen atoms at the corners [43]. Obviously, when the size of a cation (ionic radius, *r*) increases and/or decreases, more and/or fewer anions of a given size could load and pack around it, respectively. For a particular configuration, the restricting ratio of the radius may be accurately estimated by calculating the minimum allowed value for the ratio of ionic radius (*r*+/*r*-) for the arrangement to be stable. This value is an important parameter to designate the organization of the ions in the various groups of crystals. As a matter of fact, a cation is stable in a certain hole (cubic, cuboctahedral,

tetrahedral or octahedral site) only and only if it is large enough to prevent the anions from inter-touching [43]. In sum, when the cation diminishes in size, the lattice tends to stabilize, until anion-anion contact happens. Additional reduction of the lattice is hence no longer possible without a decreasing in the coordination number.

1.1.2. Synthesis of garnets

Phase diagram is a graphical representation of the physical states of a substance under different conditions of temperature and pressure. Ceramic powder treated within the Y_2O_3-Al_2O_3 composite has greatly been designed for functional and structural applications. Figure 2 displays the typical phase diagram of the Y_2O_3 – Al_2O_3 system.

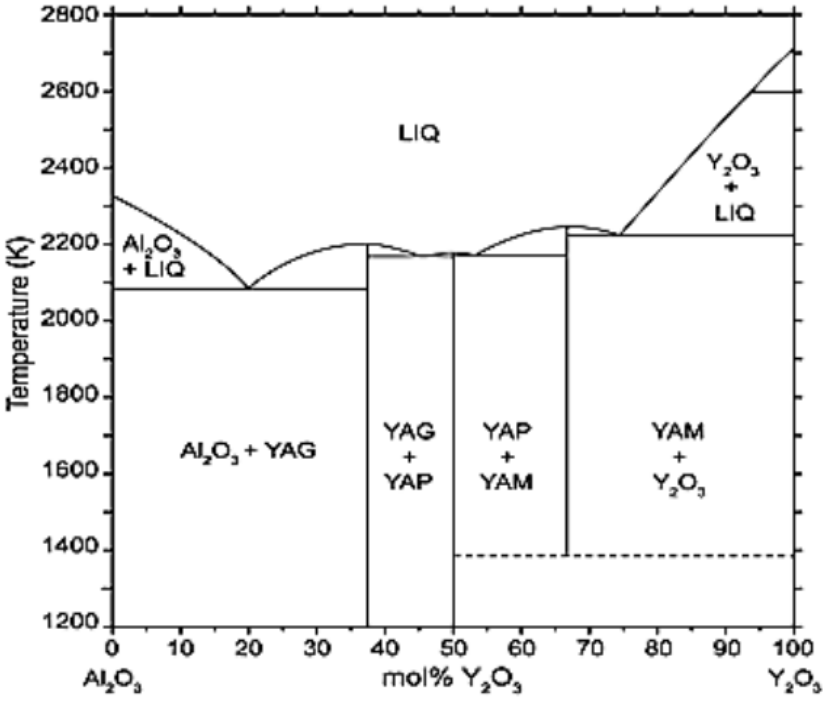

Fig. 2. Pseudo-binary phase diagram of Y_2O_3-Al_2O_3 system [38].

The Y_2O_3-Al_2O_3 phase diagram illustrates compounds of the two end members, where Y_2O_3 is cubic and Al_2O_3 is hexagonal in structure [38]. In this scheme, three stable yttrium aluminates stand with various polymorphs,

namely garnet $Y_3A1_5O_{12}$, monoclinic $Y_4Al_2O_9$, and perovskite-based orthorhombic $YAlO_3$ structure [48]. The hexagonal $YAlO_3$ has also been recognized as an intermediate metastable phase during the growth of YAG [49]. At the grain boundaries, YAG does not show any birefringence effects which in turn results in high in-line transparency when doped with rare-earth materials.

In the last decade, different processes for YAG synthesis have been successfully achieved and/or patented. All of these methods for preparing a powder of refractory non-metallic silicate materials should be classified as a function to the milieu into which the principal physicochemical mechanism is completed. This is entirely true as the very fine powders, particularly micro and nanoparticles react vigorously with their surrounding medium. Even though the majority of processes to grow these powders systematically involve various stages. The bottom line is to select the method that has a particular and controlled impact on the structure of the particle, which is obviously not simple to find. Therefore, the selection and choice of the basic method for the powder preparation is rather conditional and is habitually determined by the author of the process. The main goal of all these mentioned above techniques is to produce the materials with the lowest possible synthesis temperature, cost and by using the less-hazardous reagents.

Yttrium aluminum garnet, can be synthesized using several kind of processes including: nitrate–citrate, sol-gel, combustion [50, 51], alkoxy technology, Pechini method [52], co-precipitation [34], microwave-induced combustion [20], heterogeneous precipitation [53], hydroxide sol solutions with hydrothermal synthesis in supercritical water [46], non-hydrolytic sol–gel [17] and others.

Sol-gel method has many advantages compared to other synthesis processes, including its high reactivity, well homogeneity and the possibility to obtain a pure phase garnet structure at low temperature value [21]. In the sol-gel reaction, the sol which is consisting of nanoparticles is first obtained prior to being converted into a gel. In this view, nearly all processes of particle synthesis in a water medium could be linked to the sol-gel method, as the unreacted nanoparticles in the aqueous solution are mainly a sol and have somehow the same particle size. The sol-gel process is presently employed mostly for the synthesis of nano-powders [54]. The simplified scheme of the sol-gel technique is presented in Figure 3.

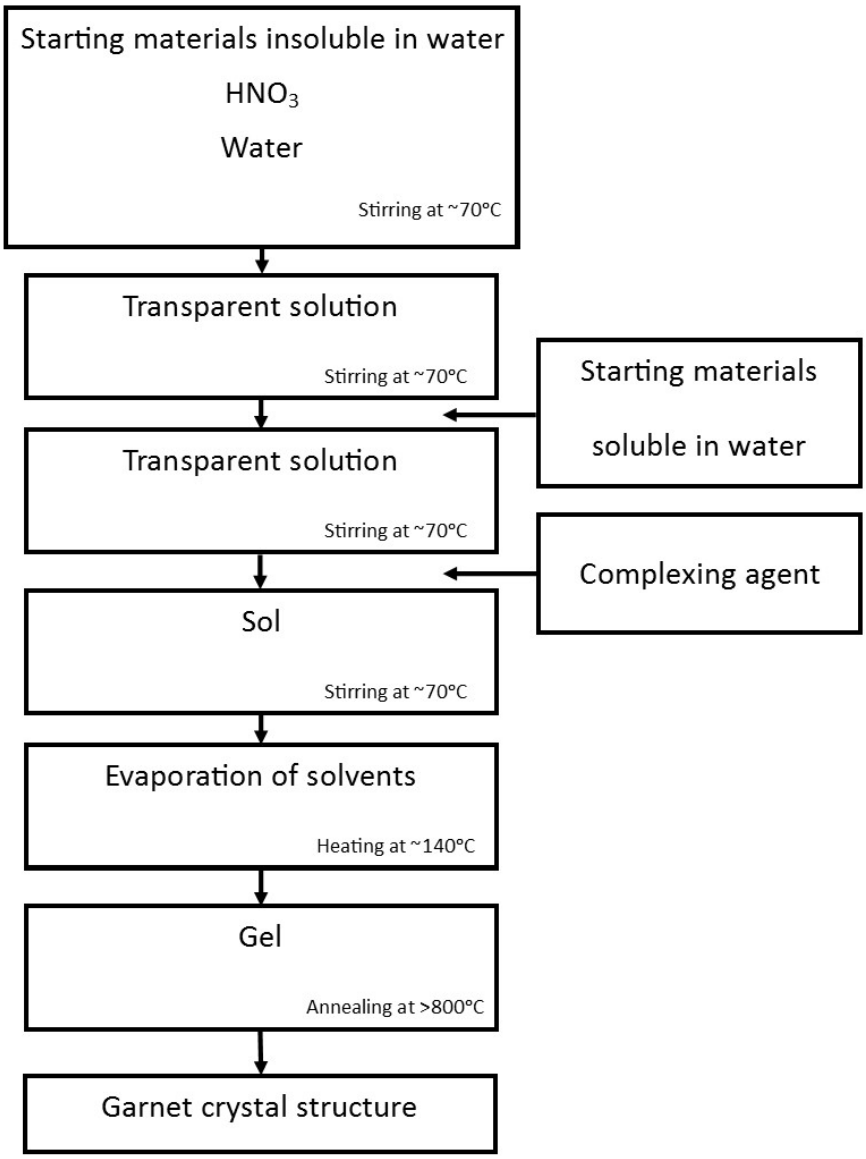

Fig. 3. Schematic representation of the steps involved in the sol-gel route.

The variation of the reaction parameters leads easily to the control of the nanoparticle size. A gel may be used straight to prepare thin films on monolithic objects. However, during the drying process and the firing step, the shrinkage could reach up to 70%, occurring thereby considerable mechanical stresses leading to the crack formation, and hence limit the method towards fabricating objects of considerable size [36, 55]. On the other hand,

employing of a gel is very efficient as a technological binder in ceramic-based technology, as the gel promotes molding, and reduces the firing temperature. A more broad method is that in which the gel is dried and converted into a xerogel, and the powder is then used for molding objects, plasma deposition, etc. [56]. Presently, the sol-gel process is employed broadly to prepare inorganic non-metallic nanoparticles. The process requires many steps which rend it somehow complicated, but at the same time, it shows a high degree of freedom and an accurate control over the final product and over it structure even at the nano-scale level. The hydrolysis of weak bases salts in a non-aqueous milieu with a solid phase of a low concentration is encouraging way as it minimizes the aggregation phenomenon of the nanoparticle and slows down considerably their growth rate, permitting thereby a better control over their structures [57]. First Yttrium aluminum garnet was synthesized by citric acid sol-gel synthesis method developed by P. Vaqueiro and M. A. Lopez-Quintela, at the University of Santiago de Compostela, Spain, in 1998. Yttrium and aluminum nitrates were chosen as starting materials. Finally, at the gelation process, the excess of water was evaporated, and the obtained sol was placed in the dryer oven at 110 °C. The obtained xerogel was then grounded to a fine powder, which was subsequently annealed at 800 °C. This temperature was found to be high enough to get pure garnet crystal structure materials [58].

One variant of the sol-gel process is the preparation of a xerogel by burning a gel. In ref. [59], Chinese scientists developed a method for preparing YAG with various concentrations of doping element at low temperature by burning the gel with citric acid as a fuel and the nitrates as oxidizing agents. This variant of a sol-gel process could also be related to the self-propagating high-temperature synthesis method with the use of a parallel oxidation reaction with a “chemical furnace” as a heat source [60]. Single-phase YAG, doped with neodymium(III) ions, was successfully grown at 850 °C without any intermediate phases, and the average size of the obtained particles was about 86 nm. This process is not a universal method, as it requires the control of the citrate-nitrate ratio which may vary considerably [61].

Pechini, an American scientist, developed a very popular method for preparing YAG material [52]. The “Pechini” method is also linked to the sol-gel family, and it is presently employed widely owing to its universality and simplicity, especially at laboratory conditions. In order to implement this synthesis method, it required the formation of stable chelate complexes with metal ions, which necessities multifunctional organic acids. Diatomic alcohols

are also needed at the first steps of this "Pechini" synthesis process and are used as a solvent, and as a participant in the polyesterification reaction at the end. The polyesterification reaction favors the formation of a polymeric 3D-network with inclusions of metal ions. In the beginning, the salt of the metal ions is dissolved in citric acid to form citrate complexes. Ethylene glycol is then added to the solution which is heated up to 100 – 130 °C to form polyester between free citric acid and ethylene glycol. After forming a fluid gel, the temperature is further increased to remove excess of alcohol molecules. The obtained viscous substance is then maintained at 450 – 600 °C for a while to remove organic substance oxidation products. The obtained precursor is a mixture of uniformly distributed metal oxides and intermediate decomposition products. Additional heat treatment helps the synthesis of nano-powder of the prescribed composition. A clear advantage of this process is its simplicity, the high degree of uniformity of the final product, the low temperature required for heat treatment, the fine nanoparticles sizes of less than 100 nm, and the possibility to use this method to prepare thin films.

Based on the "Pechini" method, different promising alternatives have been successfully developed. As a matter of fact, Korean scientists [62] synthesized YAG by citric acid alone, and the YAG phase was obtained at 800 °C. During this method, yttrium and aluminum salts were mixed in the stoichiometric composition. The citric acid solution was gently added and heated up under a continuous mixing to remove water. The solution was then dried for 24 h in a vacuum oven at 80 °C. Gel treatment was performed at a temperature of 600 °C for 6 h, which was then increased up to 900 °C for another 6 h. In ref. [63], Polish scientists proposed a way to synthesize YAG phase using acetic acid. Heat treatment at 800 °C of the starting xerogel has led to the formation of a unique YAG phase as follows: yttrium oxide was first dissolved into an acetic acid solution, heated up 60 °C and mixed for 10 h. The pH of the solution was controlled within the limit 4.5 – 5.0. Then the nitrate salt of aluminum was gently added to the solution under continuous mixing. In the final stage, ethylene glycol was poured into the solution and slowly evaporated to form a white and quasi-transparent gel. The gel was dried and converted into brown xerogel. Finally, the obtained precursor was heated up again at 800 – 1600 °C for 6 h.

An appropriate alternative to the sol-gel process is the use of metal alkoxide hydrolysis. The process is also called alkoxy technology. Alkoxides dissolve efficiently in alcohols, and they are rather easily and simply prepared. Often, it is also possible to use low purity and inexpensive metals, and

subsequently purifying the alkoxides by distillation method. Moreover, during the hydrolysis processing, the alcohol could prevent the aggregation phenomenon, and the water is then physically removed, providing thereby the transition of a sol into a gel. By hydrolysis in an alkoxide blend, the synthesis of more complex compounds it also possible [64]. During the process of converting hydroxides to oxides, the organic substance impurities are easily removed during the powder heat treatment [65]. The hydrolysis of dilute alcohol solutions of alkoxides into an excess of water solvent allows preparing nanoparticle sols that are well stable. Here again, the non-equilibrium nature of this reaction allows the synthesis of particles with nanosizes and very low volume concentration, preventing them from aggregation. In accomplishing this hydrolysis reaction of dilute alkoxides into an aqueous ethanol solution with water. However, adding water-soluble polymers or surfactants during hydrolysis reaction is a promising route to form a protective layer to the nanoparticles. Whereas a polymer is insoluble in the alcohol, it promotes the formation of a protective film at the nanoparticle surface [65].

A group from Brazil [66] proposed a new method for preparing YAG doped with europium ions through a simple microwave heating. First, chlorides of ammonium and yttrium are heated with ethanol in a flask with a reflux condenser into an argon atmosphere. Second, the obtained powders, which are alkoxides, are dried prior being heat treated into a specific microwave furnace suitable for alkoxides. The reaction time with microwaves was varied from 30 secs to 4 min, and the temperature reached about 1000 °C. According to the X-ray phase analysis, the obtained powder was a single phase YAG. This method allows decreasing the processing time for YAG phase synthesis and does not require any sophisticated and complicated equipment. However, it should be noted, that due to uneven heating particles are formed with a different size.

Aside from the YAG synthesis processes, scientists have also published the synthesis of nano-powder with supercritical conditions into an autoclave machine through hydrothermal reaction [61]. The starting elements employed were an acetic acid salt, aluminum isopropoxide and citric acid. All of these components were loaded into an autoclave with 1,4-butanediol. After heating up to 300 °C for 2 hours, a colloidal solution was formed, and was then centrifuged to obtain the powder. Among the advantages of this method are the fast synthesis reaction and the low temperature required, while the disadvantages include the need of an autoclave machine and the huge amount of the required organic components.

The cryochemical synthesis is another way to prepare the fine powders of YAG. During this reaction, first, aqueous solutions of the precursor substances are quickly frozen, then, ice from a cryogranule is removed by sublimation. In order to implement this method, French scientists, in ref. [67], used aluminum lactate, yttrium and neodymium acetates that were dissolved into boiling water, followed by adding citric acid to maintain a pH value at 4. In the opposite case, there would be precipitation of yttrium lactate, followed by the atomization of the boiling solution into liquid nitrogen. The obtained powder was placed into a vacuum sublimator. The drying process was conducted at – 20 °C during 20 h and the obtained precursor was then heated at 800 – 1200 °C. The size of the obtained agglomerates varied from 0.2 to 4 μm. One of the advantages of this process could be the very fine YAG powder obtained, and some of its main disadvantages revolve around the necessity to use organic compounds of starting components, which is a requirement for an accurate control of the medium pH; the duration time necessary for the ice removal (i.e. time–consuming method), considering the amount of liquid nitrogen, and the need for specific and costing equipment.

1.2. The applications of rare-earth ions doped and/or co-doped yttrium aluminum garnet

Stable compounds of transition elements showing a partially filled electron shell are the only one required for localized electronic transitions and sharp lines. This involves transition metals ($3d^n$, $4d^n$, or $5d^n$), rare-earth elements (also known as lanthanides) ($4f^n$).

The partially filled $4f^n$ orbital of rare-earth elements ions gives effective lines extend across the wavelength spectrum, ranging from the far–IR to the vacuum–UV. Regularly, the rare-earth ions are put separate from other transition elements. The unfilled shell of $4f^n$ electrons stays highly covered within the closed $5s^2\ 5p^6$ shells of the rare-earth ion in such a way that the optical transitions keep rather an atomic–like aspect even in a solid. This powerful shielding of the $4f^n$ electrons is in direct opposition to transition metal *d* electrons. These latter are simply in chemical bonding and are the ones which are the most impacted by the host lattice and may manifest a considerable delocalization and mixing with electronic states of other ions in the lattice. Depending on the temperature, the optical linewidths of rare–earth ions vary over a wide range of crystals. Transition line shapes are described by an inhomogeneous distribution of transition frequencies having an

inhomogeneous width, called Γ_{inh}, with each indistinguishable group or "packet" of ions having a homogeneous width Γ_h. This line structure is illustrated schematically in Figure 4.

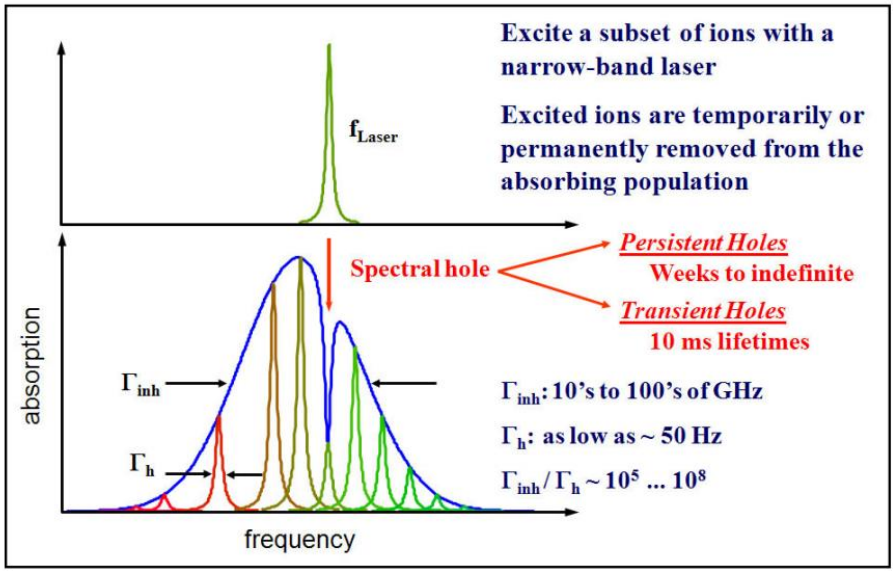

Fig. 4. Illustration of the inhomogeneous linewidth Γ_{inh} for a resonant optical material and the homogeneous linewidth Γ_h for individual groups of ions [68].

When set at room temperature, the lines are homogeneously enlarged by phonons showing a typical linewidth $\Gamma_h = 60 - 1000$ GHz ($2 - 30$ cm^{-1}); which, when settled with the wavelength representation $\lambda/\Delta\lambda$, is in the order of 10^4. As the cooling reduces the homogeneous contribution to the linewidths, they then cross over to inhomogeneous broadening which happens when temperatures are closed to 77 K. The strain and inhomogeneity of the crystal (or glass) become progressively obvious at lower temperatures, with inhomogeneous linewidth Γ_{inh} of typical values in the 1 – 30 GHz range, or even above, which is function – in case of isolated ion – of both the crystal strain and the ion concentrations that typically need to be less than 0.1 % molar. Note, that Γ_{inh} could surpass the 100 GHz when a structural disorder happens, and the narrowest homogeneous linewidths take place for the transitions occurring from the lowest component of the ground to excited multiplets. In the range of 1.5 to 10 K, which are very low temperatures obtained by cryo-coolers or by liquid helium, and when favorable cases are satisfied, for e.g. when the widths are lifetime-limited or nearly so, for the

"lowest-to-lowest" transitions, a very narrow homogeneous linewidth Γ_h can be generated (sometimes in the range of tens of Hz to a few kHz) [68-72].

A literature survey shows that there are thousands of configurations of doping and co-doping yttrium aluminum garnet. Using the same host material, it is possible to get various types of phosphors, which could be widely used in optics. Hereinafter will be discussed only a few, main applications of rare-earth ions doped/co-doped YAG synthesized by a sol-gel route.

The particular YAG:Ce^{3+} compound has been widely studied during the last few decades. This material is suitable for applications as field emission displays, scintillators, cathode-ray tubes, electroluminescent devices, afterglow materials, laser crystals and their corresponding applications [73]. One of the main property consists of the capability of YAG:Ce^{3+} to convert the blue light emitting diodes radiation into a very broad band yellow emission located at λ_{em}=~530 nm [74].

Multiples important works have indicated the important role of the YAG doped europium ions in luminescence. In fact, YAG:Eu^{3+} is a red phosphor, which can be implemented in novel optical devices, such as advanced lasers, plasma panels, radiation detectors, etc. Also YAG:Eu^{3+} like a red light phosphor can be used in fluorescent lamps or applied in agricultural lamps, which controls the growth of plants. Eu(III) ions doped in YAG matrix has few characteristic emission peaks in the range of 590 – 750 nm (from the orange tored region); the emission of europium ions corresponding to the $^5D_0 - {}^7F_j$ (j=1 – 4) electric dipole transitions [75, 76].

In recent years, many kinds of up-conversion luminescence agents, which can transform visible and infrared light to ultraviolet light and can be used in photo-catalysis reaction, had been developed. Yttrium aluminum garnet doped with Er^{3+} ions can be a very efficient up-conversion luminescence agent, transforming visible to ultraviolet light. Another optoelectronic applications - where single crystal of YAG:Er^{3+} can be used is scintillation applications, including the detection of high-energy photons and/or particles for medical imaging and security purposes (airport checkpoints, etc.). The radiation peaks can be observed at ultraviolet light region λ_{em}=250 – 400 nm [77-79].

Yb^{3+}/Er^{3+} co-doped YAG phosphors can be used as optical temperature sensors. Because of their luminescence properties, these phosphors are used as up-conversion materials. Yb^{3+}/Er^{3+} co-doped YAG has a sharp emission band gap, long lifetime, high photostability and low cytotoxicity. Due to all

these characteristics, these phosphors can be useful for bio-imaging applications, for example, photo-thermal ablation (PTA) therapy and others specific biological targets, which need to convert near-infrared optical energy to thermal one. Therefore, Yb^{3+}/Er^{3+} co-doped YAG can be used: in vivo imaging, temperature sensing and PTA of cancer cells. YAG:Yb^{3+}, like many other doped YAG phosphors, can be used as phosphor materials for solid-state lasers, optical data storage, etc. YAG:Yb^{3+} is an excellent sensitizer for the majority of the rare-earth elements and transition metals [80, 81].

Nanoparticles of YAG:Nd^{3+} have been found to have the capability of thermal sensing. These luminescent up-converter nanoparticles could be used as luminescent nano-thermometers (LNTh), where their thermal property is dependent on their particles size. It is a very interesting material for micro/nano-electronics and biological applications, where the temperature sensing is a crucial parameter. Furthermore, because of the occurring of relevant temperature singularities at their initial stages, temperature sensing could be used as an anticipated diagnosis tool for multiple diseases, for example, cancer and inflammatory processes. The biggest advantage of YAG doped neodymium ions is high quantum efficiency and the spectral region where the optical transparency of biological tissues is mainly dependent on the optical absorption. To conclude, Nd^{3+} has the faculty of a deep-tissue luminescence imaging together with the thermal sensing capability [82, 83].

Lasers of thulium doped yttrium aluminum garnet are used for non-muscle invasive bladder cancer. Different lasers are used for the treatment of tumors even at its early stages, especially, YAG:Ho^{3+} and YAG:Nd^{3+} which are selected as ideal lasers. YAG:Tm^{3+} pulsed laser has also proven to be an encouraging system to treat not only bladder tumors but also urological diseases. Different from other phosphors lasers, the YAG:Tm^{3+} can generate very sharp and well–defined incisions, furthermore its usage is more simple [80, 84].

1.3. The applications and luminescence of Tb^{3+} doped YAG

It is clearly seen that all lanthanides doped YAG practical uses have plenty of similarities. However, YAG doped with Tb^{3+} has an outstanding feature which can be used for near UV LEDs (emission from 380 to 480 nm) as a phosphor material. The incomplete occupation of the 4*f* shell is the parameter rending YAG:Tb^{3+} of a particular scientific and technological interest. The emission of Tb^{3+} originates from the main transitions $^5D_3$ and $^5D_4$. There is an emission

from the higher level $^5D_3 \rightarrow {}^7F_J$ mainly in the blue region (~370 to ~480 nm). Transitions from $^5D_3$ level are characteristic to low dopant (Tb^{3+}) concentration. Increased dopant concentration causes the cross-relaxation process and emission from $^5D_3$ level decreases. The fluorescent lines of $^5D_4$ level may be observed from ~ 480 to ~ 680 nm, which is mainly located in the green to red spectral region [21, 85, 86]. Yttrium aluminum garnet doped with terbium ions is a great candidate for practical applications such as cathode-ray tubes (CRTs), X-ray phosphors and scintillators. This phosphor is used because of its narrow-band emission spectra characteristic. YAG:Tb^{3+} has been investigated widely because of its unique green emission that can be thoroughly sensitized by using various sources, cathode-ray, UV and low-voltage excitations. Terbium ions can be excited to a $4f \rightarrow 5d$ state and can be clearly observed [1, 87, 88]. YAG:Tb^{3+} phosphor decays by emitting visible light upon UV excitation, which is the reason rending it one of the best phosphors for CRT's. YAG doped with Tb^{3+} could be synthesized using solid state reaction, co-precipitation, spray pyrolysis, sol-gel route and others [89-91]. The physical properties of YAG:Tb^{3+} depends on its synthesis method. In fact, in order to achieve high stability, luminous efficacy and efficiency, the phase purity and required particles size are required.

1.4. The applications and luminescence of Cr^{3+} doped YAG

It is known that the Nd doped YAG (YAG:Nd) is the most universally used solid-state based laser material. Habitually, approximately, the optical conversion of the lamp-pumped YAG:Nd is only about 2 – 3%. Although a laser diode (LD) pumping system can improve considerably the efficiency due to the fact that the pump light (i.e. from the LD) can be easily absorbed by the laser gain medium. However, even today, the lamp is much less expensive than the LD, hence, the lamp pumped YAG:Nd lasers are largely employed in high-power industrial applications. Therefore, it is worth considering ways of improving the efficiency of lamp pumped YAG:Nd lasers. Indeed, to do so, in 1964, a laser system based on the cross-pumped Cr^{3+} and Nd^{3+} co-doped YAG (YAG:Nd,Cr) material – was deeply investigated [92]. The sensitizer Cr^{3+} ions, have large absorption bands in the visible spectrum, in addition, their spectra overlap with the emission spectra of a Xe flash lamp. By the $^4T_2 \rightarrow {}^4A_2$ transition of Cr^{3+} ions, the energy is transferred from Cr^{3+} to Nd^{3+} ions, and consequently, the pumping efficiency is clearly improved.

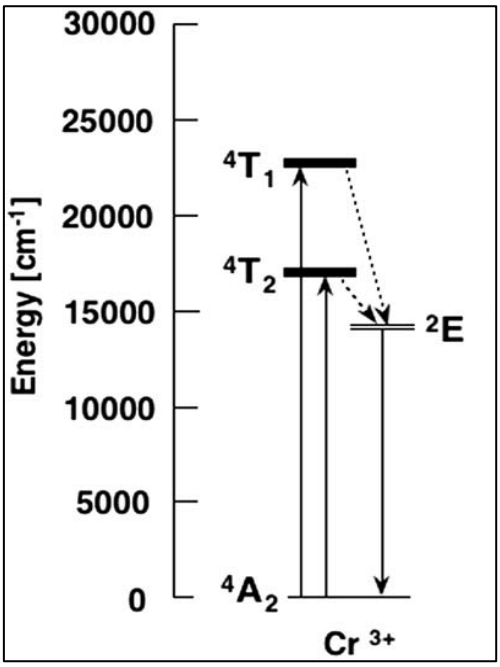

Fig. 5. Energy level diagram of chromium ions (adapted from [93])

It is well known that yttrium aluminum garnet (YAG) doped Cr^{3+} possess a broad absorption band (allowed spins) at 450 and 650 nm. These bands correspond to $^4A_2 \rightarrow {}^4T_1$ and $^4A_2 \rightarrow {}^4T_2$ excitation transitions, respectively. Emission originates in red spectral region, the $^2E \rightarrow {}^4A_2$ excitation transition originates at around 610 – 800 nm – in a far-red spectral region [44, 94]. Schematic energy level diagram of chromium (III) ions is depicted in Figure 5.

Ideally, the laser system based on this cross pumped phenomenon is beneficial for industrial lamp pumped based lasers. On the other hand, because the absorption of Cr^{3+} ions is well matched with the emission of solar light, it is also appropriate for solar pumped based lasers. The team of Kvapil reported the laser characteristics of a Cr^{3+} and Nd^{3+} co-doped YAG single crystal, where they demonstrated that the laser property was considerably improved by doping a trace amount of Cr^{3+} ions [95]. For a YAG crystal, many studies had been intensely carried out in order to investigate the characteristics of the Cr^{3+} ions luminescence and the energy transfer between Cr^{3+} and Nd^{3+} ions [96].

In the 1980s, laser based Cr^{3+} and Nd^{3+} co-doped on gadolinium scandium gallium garnet crystal was successfully developed [97]. Starting by laser

experiments employing a classical flash lamp, an improvement of the laser efficiency was clearly obtained as compared with YAG:Nd laser. Despite the fact that many theoretical and experimental studies on Cr^{3+} and Nd^{3+} co-doped lasers had already been achieved for a long time, they have not been conclusive. As a matter of fact, for a YAG crystal, it is still arduous to synthesized Cr^{3+} and Nd^{3+} co-doped YAG single crystal that is offering a high optical property. Hence, ceramic based YAG laser materials had recently become a serious alternative option to single crystals. Indeed, compared to YAG single crystals, YAG ceramics offer many advantages including the simple fabrication process, the high Nd^{3+} concentration, the effortlessness of realizing complex composite structure and especially the scalability.

A phosphor based white light emitting diode (wLED) requires broad emission band from blue to red spectral range. In order to improve wLED's luminous efficiency, it's needed to combine different monochromatic light sources, including blue, green and red. That is how wLEDs spectra can be broadened and manipulated. Doping yttrium aluminum garnet with the rare-earth ions (which emits blue and green color (for example terbium ions) and chromium ions (that emits red and far-red color)) is easily possible to get wLED phosphor materials [17, 18, 20, 53, 98].

1.5. Energy levels of Tb^{3+} and energy transfer

The electronic configuration of every rare-earth ion determines its luminescence properties. Clearly, understand the processes which take place in excited rare-earth ion, it is necessary to know the energy levels of the trivalent rare-earth ions [99]. In Figure 6 is given the energy levels of trivalent rare-earth ions, better known as a Dieke's diagram. Here will be shortly discussed the energy transfer of terbium(III) ions. Its configuration from the ground state to excited can be named interconfigural transition $[Xe]4f^8 \rightarrow [Xe]4f^7 5d^1$.

Terbium ground state is $[Xe]4f^8$, meanwhile its excited state – $[Xe]4f^7 5d^1$. Transitions $[Xe]4f^8 \rightarrow [Xe]4f^7 5d^1$ are allowed on both spins (high and low). That is the reason why terbium ions doped YAG exhibits quite a broad emission and long decay process.

Terbium ions originate the green emission spectra leaded by $^5D_4 \rightarrow {}^7F_j$ (J = 6, 5, 4, 3, 2, 1, 0) transitions. These transitions of terbium(III) ions are the main ones and determine the emitted color. It is also possible to excite the

higher-level of terbium(III) ions. $^5D_3 \rightarrow {}^7F_j$ emission occurs mainly in the blue spectral region. 5*d* orbitals are more extended than 4*f* orbitals. The spectral position of the 5*d* band is determined by few factors, including electron cloud expansion, crystal field splitting, and Stoke's shift.

Electron cloud expansion effect is observed for the metals if the effective positive charge has decreased. When the positive charge is reduced by a given negative charge on the ligands, then the d-orbitals can increase somewhat. Secondly, due to the fact that the resulting molecular orbital is formed from two atomic orbitals, the step of overlapping with ligand orbitals and the formation of covalent bonds will increase the orbital size [100].

The crystal field splitting is a static electric field resulting from the negative ligand surroundings and the positive lanthanide ions. More negative is the ligand or more positive is lanthanide ion – stronger is crystal field. Furthermore, the crystal field is depended on the lattice to which lanthanide is doped. As the doping sites are larger, the crystal field becomes weaker [101].

Stoke's shift is a phenomenon which is described as a difference in the wavelength between two most intensive peaks of emission or excitation spectra of the same electron transition. Stoke's shift is caused by the quick decay to the lowest level from which the emission occurs [102].

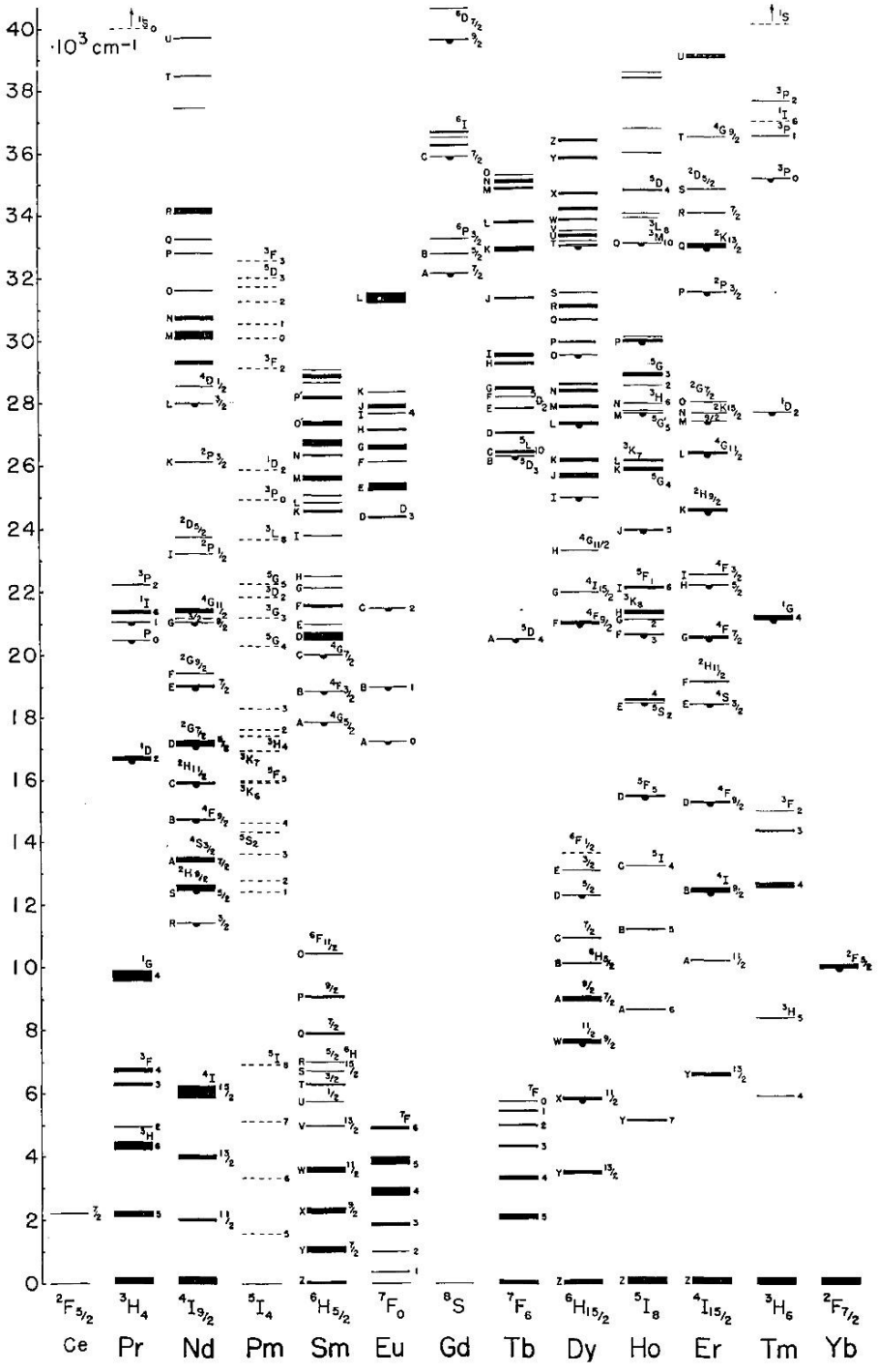

Fig. 6. Energy levels of the $4f^n$ configurations of the trivalent rare-earth ions [99]

1.6. Quantum efficiency of phosphors

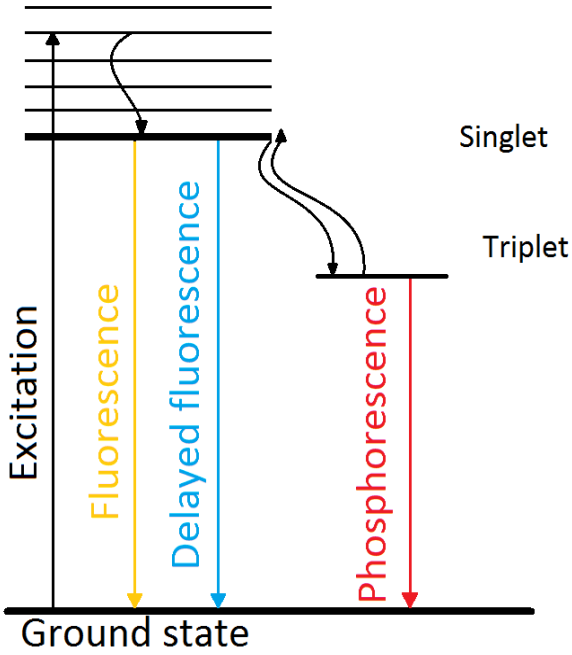

Fig. 7. Schematic diagram of the fluorescence and phosphorescence mechanism.

Quantum efficiency (QE) represents the ratio between the incident photon and the generated electron occurring into a photosensitive device. For example, in a charge coupled device (CCD), it translates the percentage % of photons hitting the photoreactive CCD surface to generate charge carriers [103]. Conventionally, it is measured either in electrons per photon or amps per watt. To probe the efficiency of a photosensitive device at each photon energy level (which is inversely proportional to its wavelength), QE is then measured over a range of different wavelengths. Note that the QE for the photons having energy below the band gap is zero. For example, while CCDs can have a QE over 90%, the photographic film shows a typical QE below 10% at some wavelengths. Indeed, the most impressive characteristics of white electroluminescent organic light-emitting devices reported so far have been accomplished in all-phosphor-doped devices, which show the potential of an IQE up to 100% [104]. The phosphorescent molecules strap the triplet

excitons that constitute 3/4 of the electron–hole pairs bound that are generated during the charge injection, and which would recombine non-radiatively in different circumstances.

In the case of a photosensitive device like a solar cell, it's worth noting that two types of quantum efficiency exist, namely, the external quantum efficiency (EQE) and the internal quantum efficiency (IQE). The EQE is the ratio between the number of charge carriers generated by the solar cell (and successfully collected) and the number of photons (at certain energy) hitting the solar cell surface (i.e. incident photons). The IQE is the ratio between the photo charges generated by the solar cell (and successfully collected) and the number of photons (hitting the solar cell surface) which are efficiently absorbed by the cell. Note that the IQE is always greater than the EQE. A low IQE is a clear indication that the solar cell is poorly absorbing the photons (i.e. the active layer within the solar cell is inefficiently using the absorbed light). To measure properly the IQE, first of all the EQE of the solar device needs to be measured, then its transmission and reflection properties, and then combining all these data to deduce the IQE.

Accordingly, the EQE relies on both the absorption capacity of the light and the collection capability of the generated charges. Upon the absorption of a photon, the electron-hole (e – h) pairs are generated, and these photo charges need to be separated prior to their successful collection. The active material of good quality should show very low recombination of e – h to minimize the drop in the external quantum efficiency.

In an ideal scenario, the quantum efficiency plot has a perfect square shape, where the QE value is quite constant over the whole measured spectrum. However, in reality, most of the solar cells QEs are reduced because of many factors, including the recombination phenomenon. In addition, all the mechanisms that impact the charges collection probability also affect the QE value. As a matter of fact, varying the state of the front solar device surface can impact the generated carrier close to the surface, and because the blue light with higher energy is easily absorbed very close to the surface, the recombination at the front surface will more affect the "blue" part of the QE. Equivalently, lower energy photon, like green or red light, is easily absorbed in the bulk of a solar cell, while a low diffusion length will influence the charge collection probability from the solar cell bulk, reducing thereby the QE in the green/red portion of the spectrum. Presently, solar cells devices available on the market commonly do not generate that much photo-power

from both UV and IR light parts (i.e. <400 nm and >1100 nm wavelengths, respectively); which are either filtered out or reabsorbed by the cell itself, which may heat up the cell (wasted energy), and could even deteriorate it [105, 106].

EQE mapping: while conventional EQE measurement is an indication of the solar device efficiency, there is sometimes the need to have a map of the EQE over larger area of the device. Indeed, this mapping supplies a powerful tool to display the homogeneity and/or the defects of the photosensitive device. Researchers from the Institute of Researcher and Development on Photovoltaic Energy (IRDEP) have realized that mapping by calculating the EQE provided by electroluminescence measurements conjugated to a hyperspectral imaging. The goal of hyperspectral imaging is to obtain the spectrum for each pixel in the image of a scene, with the purpose of finding objects, identifying materials, or detecting processes [107-111].

2. EXPERIMENTAL PART

2.1. A citric acid sol-gel synthesis method

All, in this doctoral thesis, investigated phosphors were synthesized by citric acid sol-gel method. Yttrium and terbium oxides were dissolved in hot diluted nitric acid. The obtained solution was evaporated close to dryness and a small amount of distilled water was added subsequently. Such drying procedure was repeated three times in order to remove the excess of nitric acid. Then aluminum and chromium nitrates were added and magnetically stirred for an additional 30 minutes at 70 – 80 °C. Then, the complexing agent (citric acid) at the molar ratio of 1:1 to all metal ions was added into the solution.

The formed sol was stirred for 1 h at the same temperature range. Then it was placed in the drying oven at 140 °C and left overnight. The obtained yellowish-greenish brown xerogel was ground in a mortar to fine powder. Then sample was annealed at 1000 °C for 2 h in air to remove the organic components and residual nitrates. Later it was pre-grounded and sintered at different temperatures (1200 °C, 1400 °C, 1600 °C) for 4 h in air, or 1500 °C temperature for 4 h in a reductive atmosphere (to create reductive atmosphere carbon powder was used).

2.2. Chemicals

Yttrium oxide (Y_2O_3, Aldrich, 99.99 %), aluminum nitrate ($Al(NO_3)_3 \cdot 9H_2O$, Roth, $\geq$ 98 %), chromium nitrate ($Cr(NO_3)_3 \cdot 9H_2O$, Aldrich, 99 %), terbium oxide (Tb_4O_7, Alfa Aesar 99.99 %) were used as starting materials. Citric acid ($C_6H_8O_7 \cdot H_2O$, Penta, 99.5 %) was used as the complexing agent. Carbon powder (Charcoal, Roth, p.a., powder) was used during the annealing at 1500 ^oC to support the reductive atmosphere.

2.3. Materials characterization

2.3.1. X-ray diffraction

Crystalline structures and phase purity based on the elastic scattering of X-rays from the individual atoms in the YAG powder at ambient temperature were determined by X-ray diffraction analysis. Ni-filtered Cu $K\alpha_1$ radiation with a wavelength of 1.5406 Å on Rigaku MiniFlex II and Bruker D8 Advance diffractometers were used.

Information, such as peak positions, peak intensities, and peak shape depends on the sample preparation. The powder samples were finely ground and mounted on a sample holder with a flat surface to achieve the required uniform distribution of lattice orientations. All the samples were analyzed at a step size of 0.01° increment in 2θ with a step scan of 1 s and the XRD patterns were recorded from 10° to 70° degree angle of 2θ (scan speed 10°/min). Purity of all samples were identified with the use of the program *Match*. Tb^{3+} doped YAG systems was refined by the Rietveld profile method with the use of the program *Fullprof*. Rietveld refinement XRD scan speed was 3.5 °/min

2.3.2. TG analysis

Thermal analysis of the YAG and doped/co-doped YAG gel were carried out in the air flow. The powders were weighed from ~5 mg to ~10 mg and placed into a platinum sample holder. Thermogravimetric analysis (TGA) were recorded between 30 °C and 950 °C range at a ramp rate of 10 °C/min using simultaneous thermal analyzer STA6000 from PerkinElmer. An empty platinum holder was used as a reference. The instrument measures the weight loss between the sample and the reference.

2.3.3. SEM analysis

The morphology of annealed and sintered YAG samples were analyzed using FEGSEM (Field Emission Gun Scanning Electron Microscope) Hitachi SU-70 at different magnifications. The Hitachi SU-70 is scanning electron microscope, providing 1 nm resolution, 0.5 to 30 kV accelerating voltage, field immersion operation, and energy filtered BSE detector.

During the analysis powder sample was sprinkled onto a conducting carbon film mounted on aluminum stubs. A secondary electron lower detector operated at 2 kV accelerating voltage was used to obtain images of the powder. Working distance was around 10 mm.

2.3.4. Luminescence investigations

Luminescence spectra were recorded on the Edinburgh Instruments FLS980 spectrometer equipped with double excitation and emission monochromators, 450 W Xe arc lamp, a cooled (-20 °C) single-photon counting photomultiplier (Hamamatsu R928) and a lens optics for powder samples. The photoluminescence emission spectra were corrected by a correction file obtained from a tungsten incandescent lamp certified by National Physics

Laboratory, UK. For recording excitation and emission, slits were set to 0.5nm. Step size was 0.5 nm and integration time was 0.2 s. The photoluminescence decay curves were measured under Xe μ-flash lamp μF920 excitation. Excitation wavelengths of 273 and 600 nm were selected while emission was monitored at 543 and 688 nm.

2.3.5. EQE calculations

External quantum efficiencies were calculated by measuring emission spectrum of the $BaSO_4$ sample in a Teflon coated integration sphere. Excitation wavelengths were 273, 430, and 600 nm, and emission spectra were recorded in the ranges of 250 − 800, 410 − 800, and 580 − 800 nm, respectively. The excitation and emission slits were set to 4 nm. Step width was 0.5 nm, and integration time was 0.4 s. The same measurements were repeated for the phosphor samples. The EQE values were obtained by employing the following formula [76]:

$$EQE = \frac{\int I_{em,\,sample} - \int I_{em,\,BaSO_4}}{\int I_{ref,\,BaSO_4} - \int I_{ref,\,sample}} \times 100\% \qquad \text{(Eq. 1.)}$$

Here, $\int I_{em,\,sample}$ and $\int I_{em,\,BaSO_4}$ are integrated emission intensities of the phosphor sample and $BaSO_4$, respectively. $\int I_{ref,\,BaSO_4}$ and $\int I_{ref,\,sample}$ are the integrated reflectance of the $BaSO_4$ and phosphor sample, respectively. The EQE measurements for each sample were repeated five times in order to get some statistical data. All measurements were performed at room temperature and ambient pressure in air unless specified otherwise [76].

2.3.6. CIE color coordinates calculations

Color coordinates in CIE 1931 color space diagrams were calculated from emission spectra employing the Edinburgh Instruments F980 software (version 1.3.1).

3. RESULTS AND DISCUSSIONS

3.1. Initial investigation of doping effect of Tb^{3+} ions on $Y_3Al_5O_{12}:Cr^{3+}$ phosphor

3.1.1. Structural properties and morphology

Termogravimetric (TG) curves of Y-Al-O xerogel are presented in Figure 8. TG curve of annealed sample indicates that there are four main steps of the mass loss. The first mass loss at 100 °C in the DTG (diferential termogravimetric) curve can be related to evaporation of the absorbed water. The second mass loss at 201 °C in the DTG curve is due to pyrolysis and decomposition of nitrates occurring during the further heating of analyzed Y-Al-O xerogel. The third (427 °C) and the fourth peaks (618 °C) are weaker and broader. These mass losses correspond to decomposition of volatile citric acid and nitrates [21, 94, 112-114]. There is no mass changes when the temperature is raised above ~800 °C. This indicates that the target phase formation is finished. Nevertheless, all samples were synthesized at higher temperatures in order to obtain better luminescence properties. The TG curves of all doped and co-doped xerogels showed the same behavior, therefore, they are not represented in this chapter.

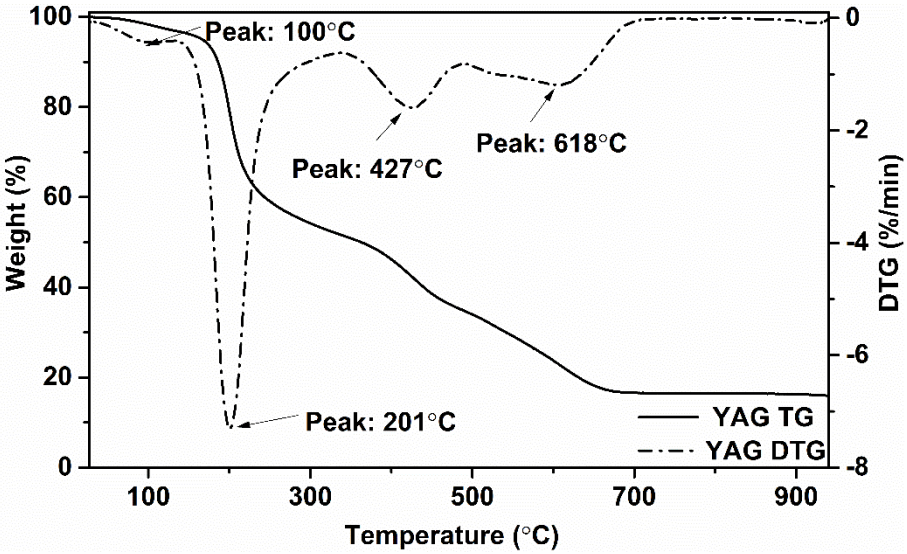

Fig. 8. TG curves of Y-Al-O xerogel obtained after the drying process.

XRD patterns of YAG powders annealed at different temperatures in the air are presented in Figure 9. Each peak matches well the reference pattern of yttrium aluminum garnet (PDF2 [00-033-0040]). It is obvious, that 1000 °C temperature is high enough to yield single phase cubic garnet structure, corresponding to space group $Ia\bar{3}d$ (#230). However, the XRD signals of samples annealed at 1000 °C are rather broad. Raising the synthesis temperature from 1000 to 1600 °C resulted in much narrower peaks indicating that the size of synthesized particles increased.

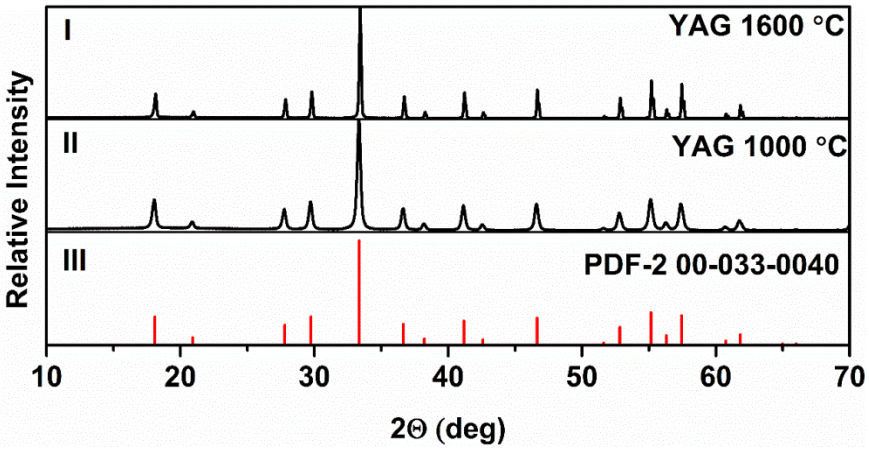

Fig. 9. XRD patterns of YAG synthesized at different temperatures (1000 (II) and 1600 °C (I)) in air and reference pattern (III).

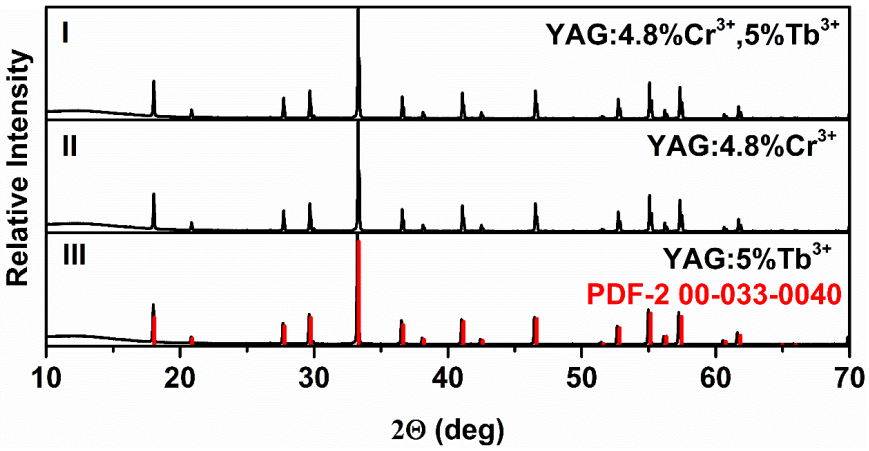

Fig. 10. XRD patterns of doped and co-doped YAG sintered at 1600 °C: YAG:4.8%Cr^{3+},5%Tb^{3+} (I), YAG:4.8%Cr^{3+} (II), YAG:5%Tb^{3+} with YAG reference pattern (III).

The XRD patterns presented in Figure 10 showed that doping and co-doping by Tb and/or Cr ions does not affect the phase formation. The ions were successfully introduced into the garnet lattice since each peak of patterns matches well with the reference data of YAG (PDF2 00-033-0040).

The morphology features of YAG annealed at different temperatures, chromium or terbium doped YAG and terbium-chromium co-doped YAG samples annealed at 1600 °C were inspected by taking scanning electron microscopy (SEM) images. The micrographs are represented in Figure 11 and Figure 12.

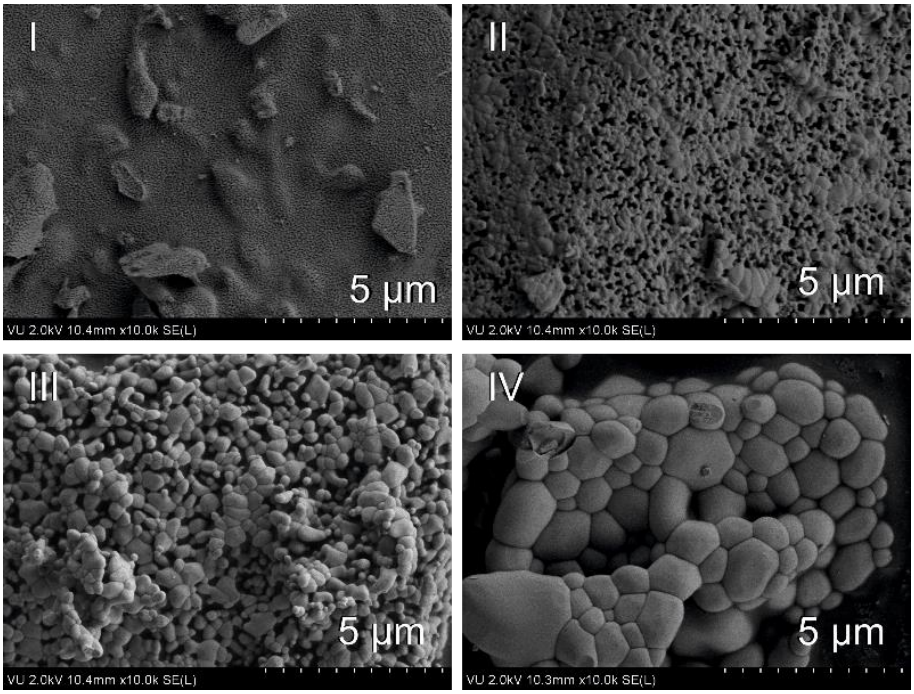

Fig. 11. SEM images of YAG synthesized at different temperatures: 1000 °C (I), 1200 °C (II), 1400 °C (III) and 1600 °C (IV).

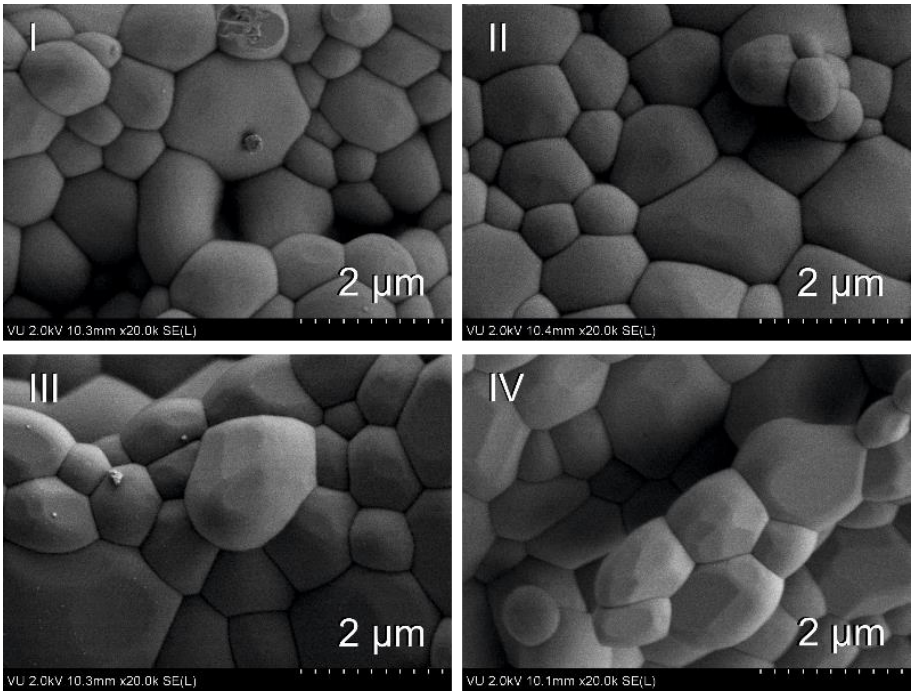

Fig. 12. SEM images of materials sintered at 1600 °C: YAG (I), YAG:5%Tb^{3+} (II), YAG:4.8%Cr^{3+} (III) and YAG:4.8%Cr^{3+},5%Tb^{3+} (IV).

All analyzed samples possess well-shaped irregular sphere-like morphology. During the annealing process, the partly molten nanosheets become cross-linked causing highly agglomerated particles. The presence of pores is clearly visible, which could be formed due to the escaping gasses during the burning of organic components and residual nitrates. In addition, it is obvious that the increase of the synthesis temperature from 1000 to 1600 °C results in the growth of particles. This goes hand in hand with the peak narrowing observed in the XRD patterns for the materials synthesized at elevated temperatures.

It is also clear that doping does not affect the morphology of samples. There are no significant differences in the SEM pictures for the samples with the different content of dopant ions as seen in Figure 12. The micro-size agglomerates maintain well-shaped irregular sphere-like morphology regardless the chemical composition.

3.1.3. Optical properties

The excitation, emission and reflection spectra of YAG:5%Tb^{3+}, YAG:4.8%Cr^{3+}, YAG:4.8%Cr^{3+},5%Tb^{3+} are depicted in Figure 13, Figure 14 and Figure 15, respectively.

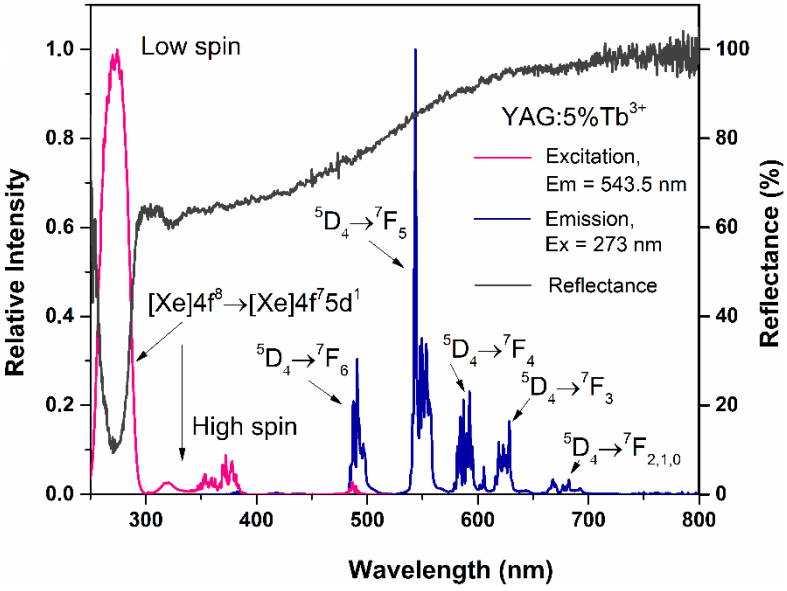

Fig. 13. Excitation, emission and reflection spectra of YAG:5% Tb^{3+} sintered at 1600 °C.

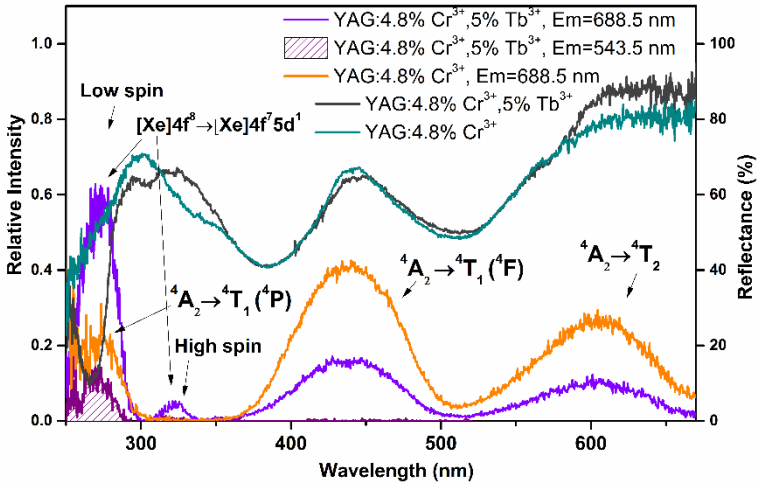

Fig. 14. Excitation spectra of YAG:4.8%Cr^{3+},5%Tb^{3+} (emission at 688.5 and 543.5 nm) and YAG:4.8%Cr^{3+} (emission at 688.5 nm) sintered at 1600 °C, and reflection spectra of YAG:4.8%Cr^{3+},5%Tb^{3+} and YAG:4.8%Cr^{3+}.

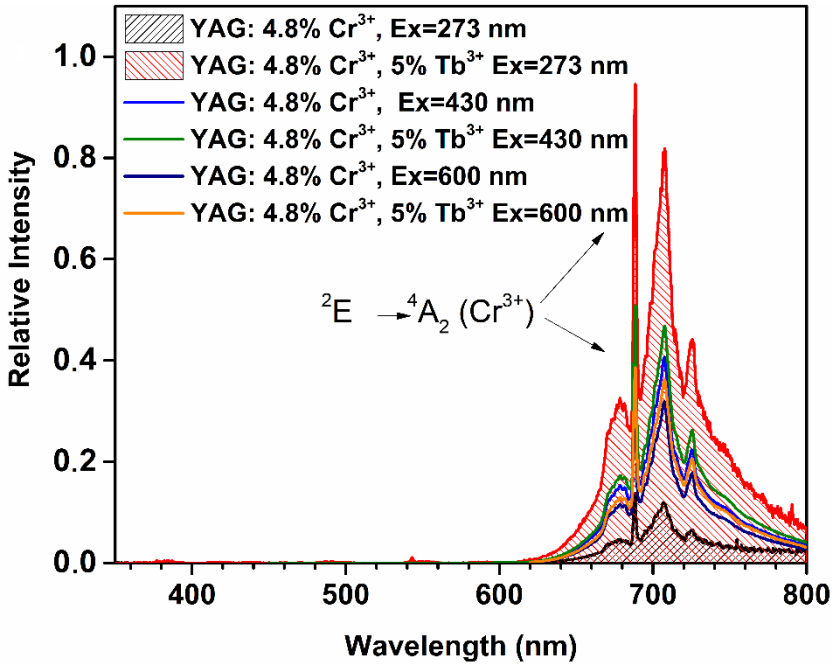

Fig. 15. Emission spectra of YAG:4.8%Cr^{3+},5%Tb^{3+} and YAG:4.8%Cr^{3+}annealed at 1600°Cand excited by 273 nm, 430 nm or 600 nm light, respectively.

Excitation spectrum of YAG:5% Tb^{3+} recorded for 543.5 nm emission is shown in Figure 13. The bands with the maximum at 273 and 317 nm are attributed to the low and high spin transitions [Xe]$4f^8$ → [Xe]$4f^75d^1$ of Tb^{3+}, respectively [115]. The emission spectrum was recorded for 273 nm excitation. There can be clearly observed peaks, which can be associated with Tb^{3+} transitions. The emission spectrum exhibits peaks corresponding to $^5D_4 \rightarrow {}^7F_6$ (at 480–510 nm (maximum at 491 nm), blue region), $^5D_4 \rightarrow {}^7F_5$ (at 535–565 nm (maximum at 543 nm), green region), $^5D_4 \rightarrow {}^7F_4$ (at 580–610 nm (maximum at 592 nm), orange region), $^5D_4 \rightarrow {}^7F_3$ (610–635 nm (maximum at 628 nm), red region) and $^5D_4 \rightarrow {}^7F_{2,1,0}$ transitions are not very intensive, but they are in red region (667–692 nm range). The most intensive peak is located at 543.5 nm. This yields a green-yellowish emission color. Results of excitation spectrum correlate well with the reflectance data. The maximum of the bands in the excitation spectrum matches the minimum in reflectance spectrum.

All Tb^{3+} transitions, mentioned above, are quenched in terbium-chromium co-doped YAG excitation spectrum recorded for 543.5 nm emission as depicted in Figure 14. Meanwhile, the $^4A_2 \rightarrow {}^4T_2$, $^4A_2 \rightarrow {}^4T_1$ (^4F) and $^4A_2 \rightarrow {}^4T_2$ (^4P) transitions of Cr^{3+} dominate in the excitation spectra of YAG:4.8%Cr^{3+} (λ_{em} = 688.5 nm; Fig. 14). The $^4A_2 \rightarrow {}^4T_2$ (^4P) transitions of Cr^{3+} overlapping with [Xe]$4f^8 \rightarrow$ [Xe]$4f^7 5d^1$ low spin transition of Tb^{3+} turns to the most expressed in the YAG:4.8%Cr^{3+},5%Tb^{3+} excitation spectrum (λ_{em} = 688.5 nm). Even the high spin [Xe]$4f^8 \rightarrow$ [Xe] $4f^7 5d^1$ transition of Tb^{3+} are observed in the YAG:4.8%Cr^{3+},5%Tb^{3+} excitation spectrum recorded for 688.5 nm emission. This clearly indicates that energy transfer occurs from Tb^{3+} to Cr^{3+} ions.

In Figure 15 emission spectra of doped and co-doped YAG annealed at 1600°C and excited 273 nm, 430 nm or 600 nm light, respectively, are depicted. YAG:4.8%Cr^{3+} and YAG:4.8%Cr^{3+},5%Tb^{3+} phosphors have a wide band in the red and far-red regions (620–800 nm). The maximum of emission at 688.5 nm is contributed by the $^2E \rightarrow {}^4A_2$ transition of Cr^{3+} ions in YAG:4.8%Cr^{3+} and YAG:4.8%Cr^{3+},5%Tb^{3+}. Co-doping YAG:4.8%Cr^{3+} with terbium leads to the slightly higher intensities of Cr^{3+} emission upon 430 and 600 nm excitation. Meanwhile, more than the six-fold increase of Cr^{3+} emission intensity is observed upon 273 nm excitation of YAG:4.8%Cr^{3+} co-doped with terbium ions when compared to the YAG doped solely with Cr^{3+} ions. Such behavior implies that energy absorbed by Tb^{3+} ions is transferred to Cr^{3+} ions leading to higher intensities of Cr^{3+} emission lines/bands.

Luminescence properties were further investigated by (co-)dopant-dependent luminescence lifetime measurements of YAG:5%Tb^{3+}, YAG:4.8%Cr^{3+}, YAG:4.8%Cr^{3+},5%Tb^{3+} (Fig. 16, Fig. 17, and Fig. 18. Table.1, Table.2. and Table.3.).

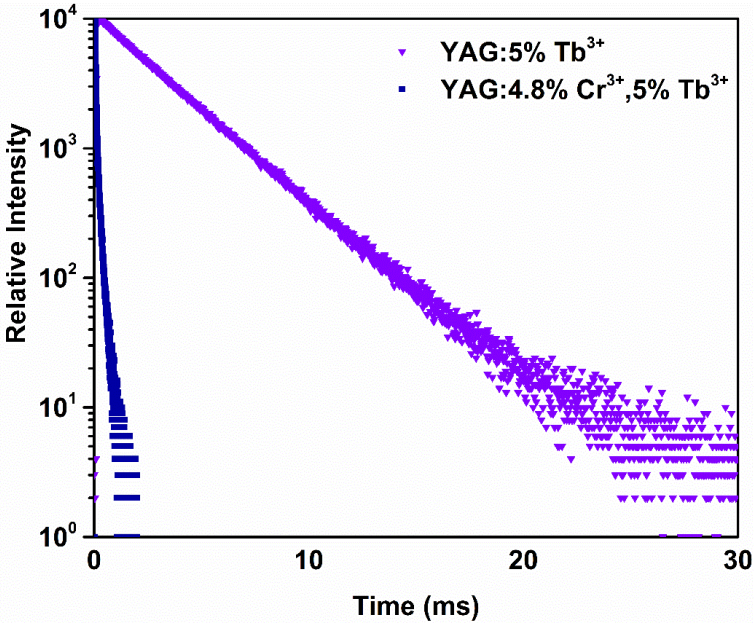

Fig. 16. Luminescent decay curves of YAG:5%Tb^{3+} and YAG:4.8%Cr^{3+},5%Tb^{3+} recorded at 543.5 nm upon excitation at 273 nm

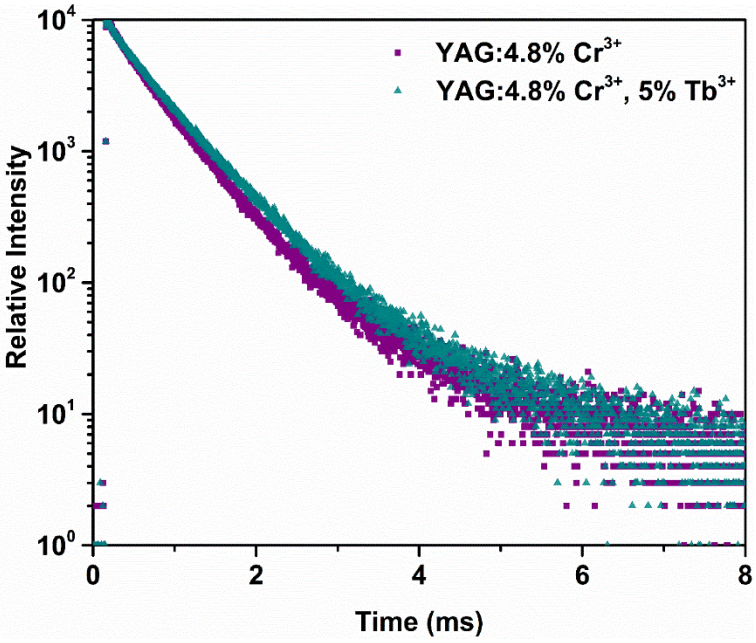

Fig. 17. Luminescent decay curves of YAG:4.8%Cr^{3+} and YAG:4.8%Cr^{3+},5%Tb^{3+} recorded at 688.5 nm upon excitation at 430 nm

Table 1. Decay times of YAG:5%Tb^{3+} and YAG:4.8%Cr^{3+},5%Tb^{3+}, λ_{ex}=273 nm, λ_{em}=543.5 nm

Sample	**τ_1,ms**	**τ_1,%**	**τ_2,ms**	**τ_2,%**	**$\tau_{average}$**
1. YAG:5%Tb^{3+}	3.0	100	0	0	3.0
2.YAG:4.8%Cr^{3+},5%Tb^{3+}	0.07	47	0.25	53	0.17

Table 2. Decay times of YAG:4.8%Cr^{3+} and YAG:4.8%Cr^{3+},5%Tb^{3+}, λ_{ex}=430 nm, λ_{em}=688.5 nm.

Sample	**τ_1,ms**	**τ_1,%**	**τ_2,ms**	**τ_2,%**	**$\tau_{average}$**
1. YAG:4.8%Cr^{3+}	0.4	73	0.9	27	0.5
2. YAG:4.8%Cr^{3+},5%Tb^{3+}	0.5	68	0.9	32	0.6

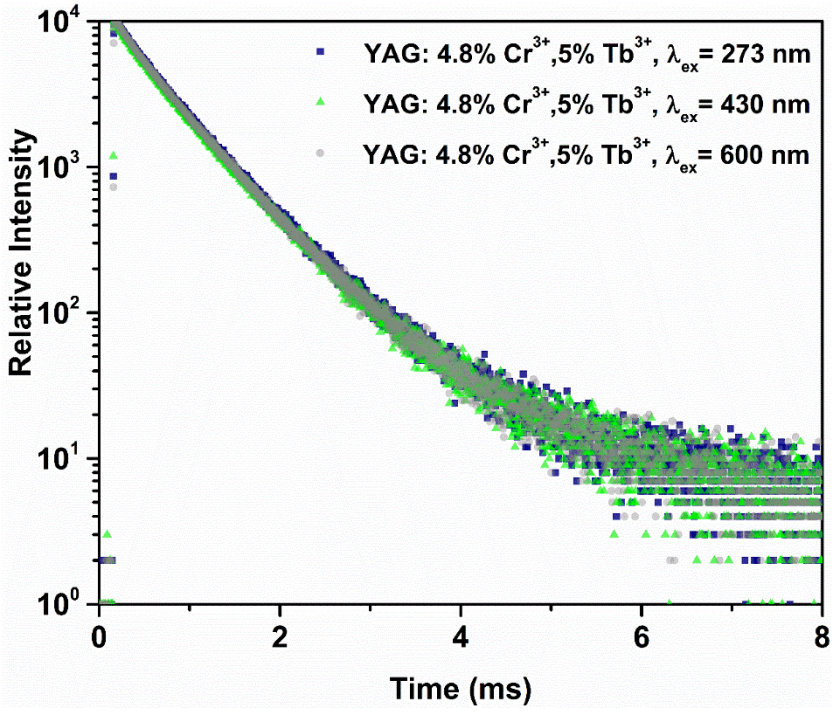

Fig. 18. Luminescence decay curves of YAG:4.8%Cr^{3+},5%Tb^{3+}, recorded at 688.5 nm upon excitation at 273 nm, 430 nm or 600 nm respectively.

Table 3. Decay times of YAG:4.8%Cr^{3+},5%Tb^{3+}, λ_{ex}=273 nm, λ_{ex}=430 nm, λ_{ex}=600 nm, λ_{em}=688.5 nm.

Sample	**τ_1,ms**	**τ_1,%**	**τ_2,ms**	**τ_2,%**	**$\tau_{average}$**
1. YAG:4.8%Cr^{3+},5%Tb^{3+} λ_{ex}=273nm	0.5	68	1.0	32	0.7
2. YAG:4.8%Cr^{3+},5%Tb^{3+} λ_{ex}=430nm	0.5	68	1.0	32	0.7
3. YAG:4.8%Cr^{3+},5%Tb^{3+} λ_{ex}=600nm	0.5	70	1.0	30	0.6

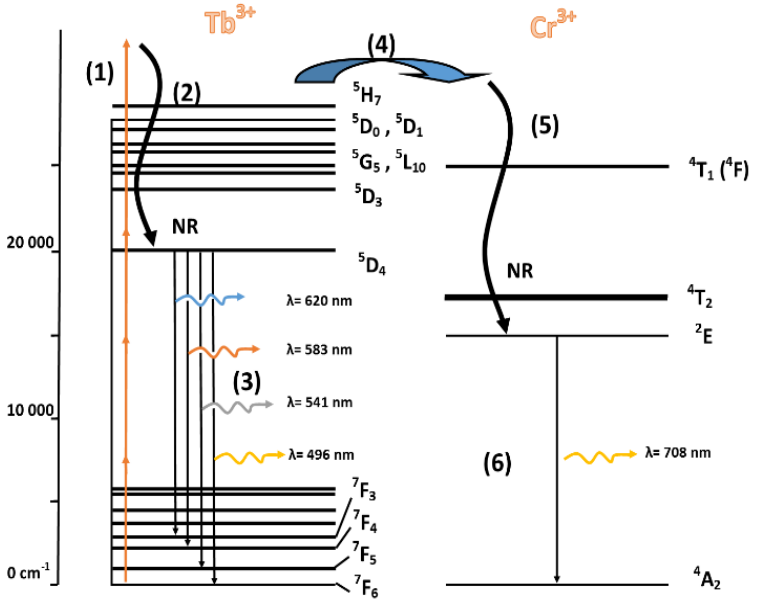

Fig. 19. Proposed mechanism for energy transfer and photoluminescence in terbium-chromium co-doped YAG.

In Figure 16 it can be clearly observed a dramatic decrease of the luminescence lifetime. The mono-exponential Tb^{3+} decay time value of approximately 3.0 ms (Table 1.), observed for YAG:5%Tb^{3+}, is in a good

accord with literature values [86]. The lifetime of Tb^{3+} in YAG:4.8%Cr^{3+},5%Tb^{3+} becomes the bi-exponential parameter and it is shortened to 0.17 ms ($\tau_{average}$) (Table 1.). It could be because of the Cr^{3+}ions concentration in the sample. Meanwhile, in Figure 17, the lifetime of the samples is rather much alike and there is no such a big difference between analyzed samples. But the bi-exponential lifetime of Cr^{3+} ions in co-doped sample becomes slightly longer than in YAG:4.8%Cr^{3+}. The longer decay times could be attributed to the increase of the internal efficiency of activator (Tb^{3+}) ions. The lifetime value of YAG:4.8%Cr^{3+} is 0.5 ms and the lifetime value of the YAG:4.8%Cr^{3+},5%Tb^{3+} is 0.6 ms (Table 2.). [19]. However, the lifetime of Cr^{3+} in YAG:4.8%Cr^{3+},5%Tb^{3+} recorded at 688.5 nm upon excitation at 273, 430 and 600 nm, respectively (Figure 18.), does not change a lot ($\tau_{average}$ from 0.6 to 0.7 ms) (Table 3.). It can be because of the same value of the activators Cr^{3+} ions.

In order to summarize the results, presented in this chapter, we propose a mechanism for energy transfer and luminescence processes for the co-doped YAG (Figure 19.). The mechanism consists of (1) absorption of 273 nm light and $[Xe]4f^8 \rightarrow [Xe]4f^7 5d^1$ low spin transitions of Tb^{3+} electrons; (2) non-radiative cross-relaxation process to $^5D_4$ level of Tb (III) ion; (3) radiative energy transfer from the excited $^5D_4$ state to the ground levels of ^7F_J; (4) non-radiative energy transfer from the excited $[Xe]4f^75d^1$ state of Tb (III) ion to $^4T_1$ (^4P), $^4T_1$ (^4F), $^4T_2$ or/and ^2E level of Cr (III) ion; (5) non-radiative cross-relaxation process to ^2E level of Cr (III) ion; (6) radiative energy transfer from the excited ^2E state to the ground level of $^4A_2$. Note, that non-radiative energy transfer from any excited state of Tb (III) ion may occur to other levels of excited Cr (III) ion, nevertheless the energy transfer from $[Xe]4f^75d^1$ (Tb^{3+}) to $^4T_1$ (^4P) (Cr^{3+}) is very likely, since the energy of excited states of Tb (III) and Cr (III) ions is very close (~ 37 000 cm^{-1} and ~ 36 000 cm^{-1}, respectively). The shortened lifetime, the quenched whole emission of Tb^{3+} and the enhanced emission of Cr^{3+} upon 273 nm excitation imply that the energy transfer from Tb^{3+} to Cr^{3+} is the nonradiative process.

3.2. An optimal concentration of Cr^{3+} ions in doped and co-doped $Y_3Al_5O_{12}$

3.2.1. Phase formation

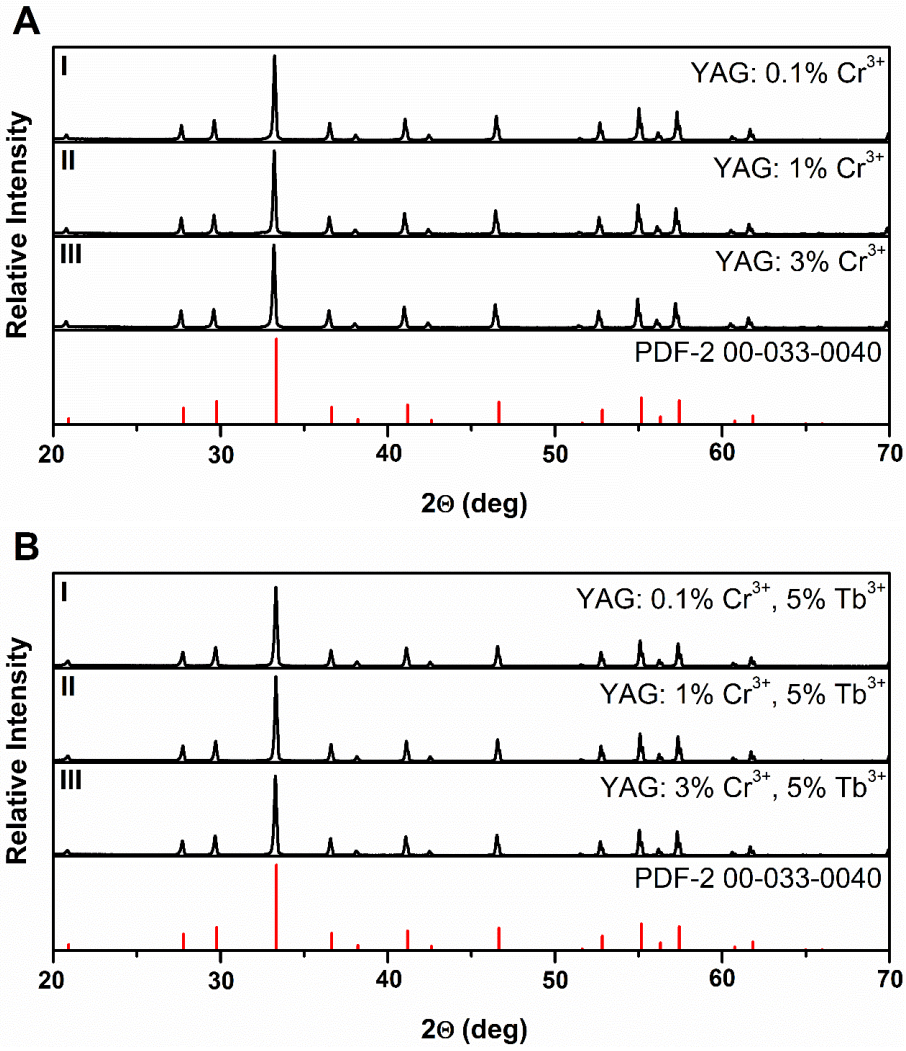

Fig. 20. XRD patterns of YAG:0.1%Cr^{3+} (A-I), YAG:1% Cr^{3+} (A-II), YAG:3% Cr^{3+} (A-III), and YAG:0.1%Cr^{3+},5%Tb^{3+} (B-I), YAG:1%Cr^{3+},5%Tb^{3+} (B-II), YAG:3%Cr^{3+},5%Tb^{3+} (B-III), sintered at 1500 °C in reducing atmosphere.

The synthesized samples of doped and co-doped YAG were analyzed by the XRD method. XRD patterns of YAG powders sintered at 1500 °C in reducing

atmosphere together with standard XRD data (PDF2 [00-033-0040]) are presented in Figure 20. Each observed peak matched the standard XRD data. That means that all (co-)doped YAG samples are single phase and possess a cubic garnet crystal structure, which corresponds to the space group $Ia\bar{3}d$ (#230).

3.2.2. Optical properties

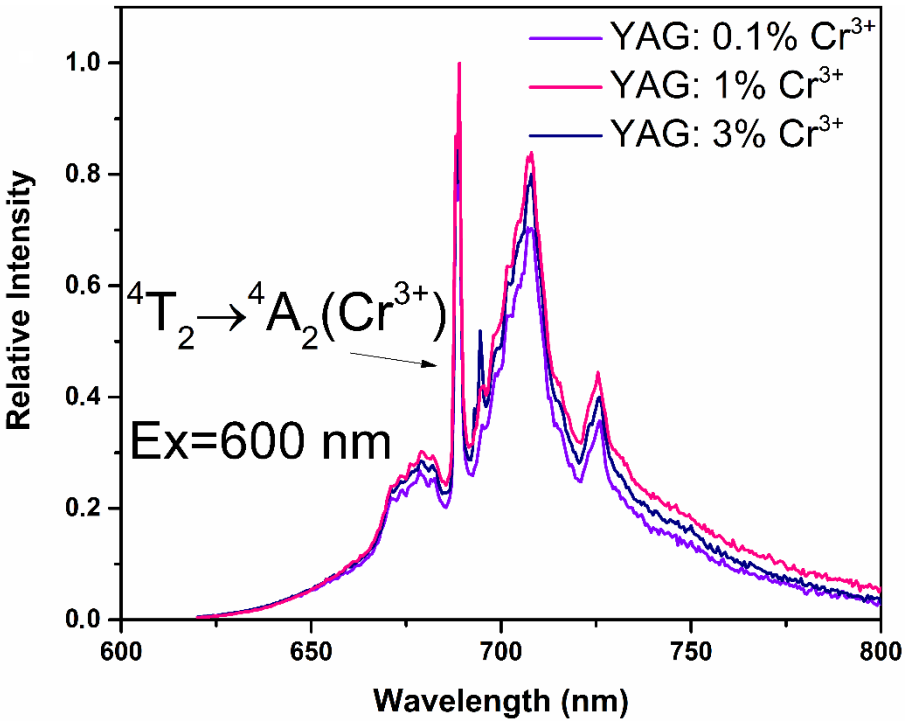

Fig. 21. Emission spectra (λ_{ex} = 600 nm) of YAG:0.1%Cr^{3+}, YAG:1%Cr^{3+} and YAG:3%Cr^{3+}.

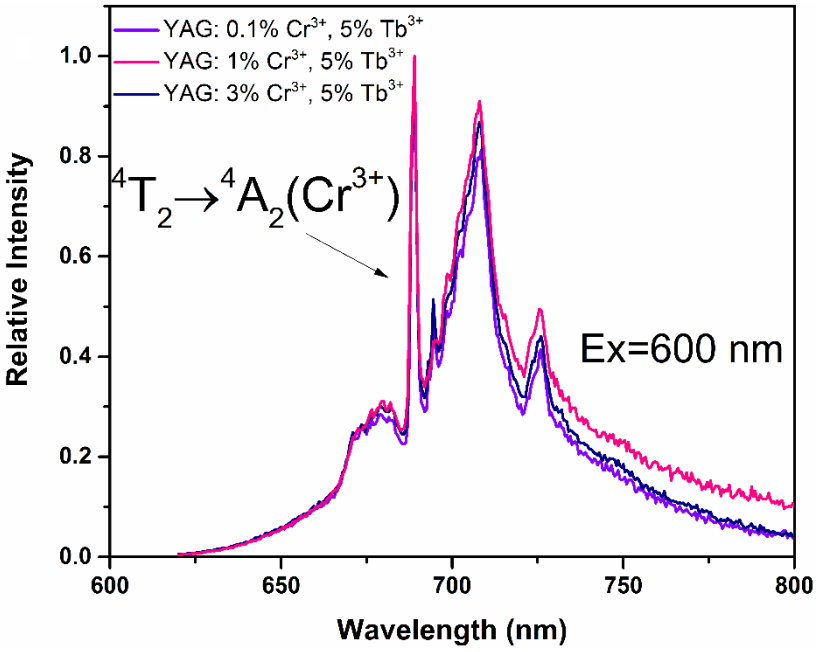

Fig. 22. Emission spectra (λ_{ex} = 600 nm) of YAG:0.1%Cr^{3+},5%Tb^{3+}, YAG:1%Cr^{3+},5%Tb^{3+}, and YAG:3%Cr^{3+},5%Tb^{3+}.

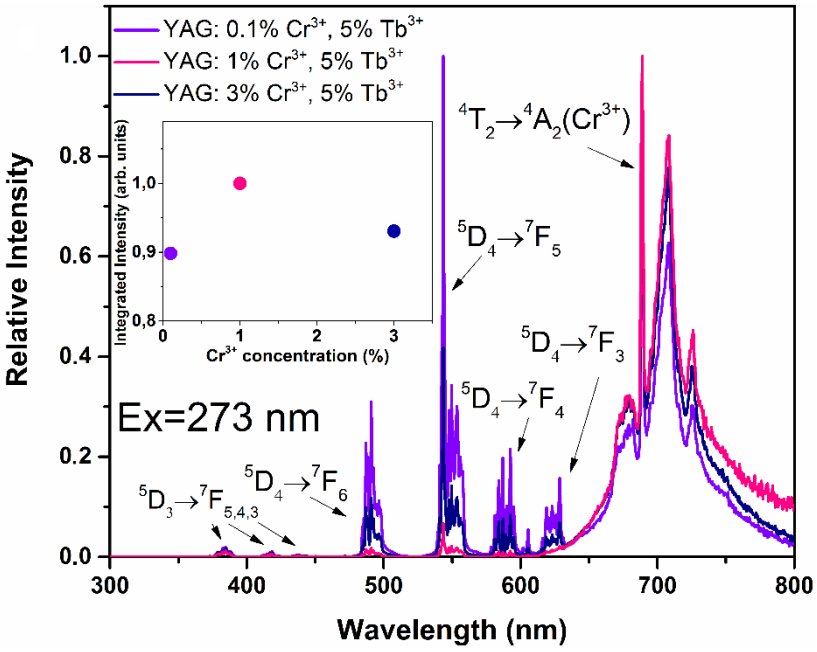

Fig. 23. Emission spectra (λ_{ex} = 273 nm) of YAG:0.1%Cr^{3+},5%Tb^{3+}, YAG:1%Cr^{3+},5%Tb^{3+}, and YAG:3%Cr^{3+},5%Tb^{3+}.

All doped and co-doped phosphors excited by 600 nm (Figure 21. and Figure 22, respectively) radiation possess a wide emission band at 620-800 nm, which is attributed to $^4T_2 \rightarrow {}^4A_2$ transition of Cr^{3+} ions. Doped and co-doped phosphors containing 1% Cr^{3+} ions exhibit the highest emission intensity. It means that doping YAG with 1% Cr^{3+} is optimal dopant concentration in the lattice.

Emission spectra of co-doped YAG:*x*%Cr^{3+},5%Tb^{3+} (*x*=0.1, 1, 3) samples excited at 273 nm are presented in Fig. 23. The transitions originating from the $^5D_3$ excited state of terbium ions are visible for all co-doped samples (YAG:*x*%Cr^{3+},5%Tb^{3+} (*x*=0.1, 1, 3)), as well as, transitions from the $^5D_4$ excited state are characteristic for all samples too. The emission band from nearly 400 nm to ~620 nm is habitual to terbium ions emission. In this band, the most intensive peaks belong to YAG:0.1%Cr^{3+},5%Tb^{3+} sample. Investigating only this band, it can be found that increasing chromium ion concentration emission decreases. It might happen because the energy is transferred to chromium ions. However, a wide emission band at 620 – 800 nm, which is attributed to $^4T_2 \rightarrow {}^4A_2$ transition of Cr^{3+} ions, the most intensive peak belongs to YAG:1%Cr^{3+},5%Tb^{3+} sample. Investigating this band, it can be found that increasing Cr^{3+} concentration emission increases (max 1% Cr^{3+}). Further increase of the Cr^{3+} concentration leads to noticeable emission quenching (concentration quenching). Nevertheless, from the integrated emission intensity it is clearly visible that the largest calculated area contains YAG:1%Cr^{3+},5%Tb^{3+} sample. It means that YAG co-doped with 1% Cr^{3+} is optimal dopant concentration with the respect to the highest emission value.

3.3. External quantum efficiency dependence on dopant (Tb^{3+}) concentration in $Y_3Al_5O_{12}$:1%Cr^{3+}

3.3.1. Phase formation

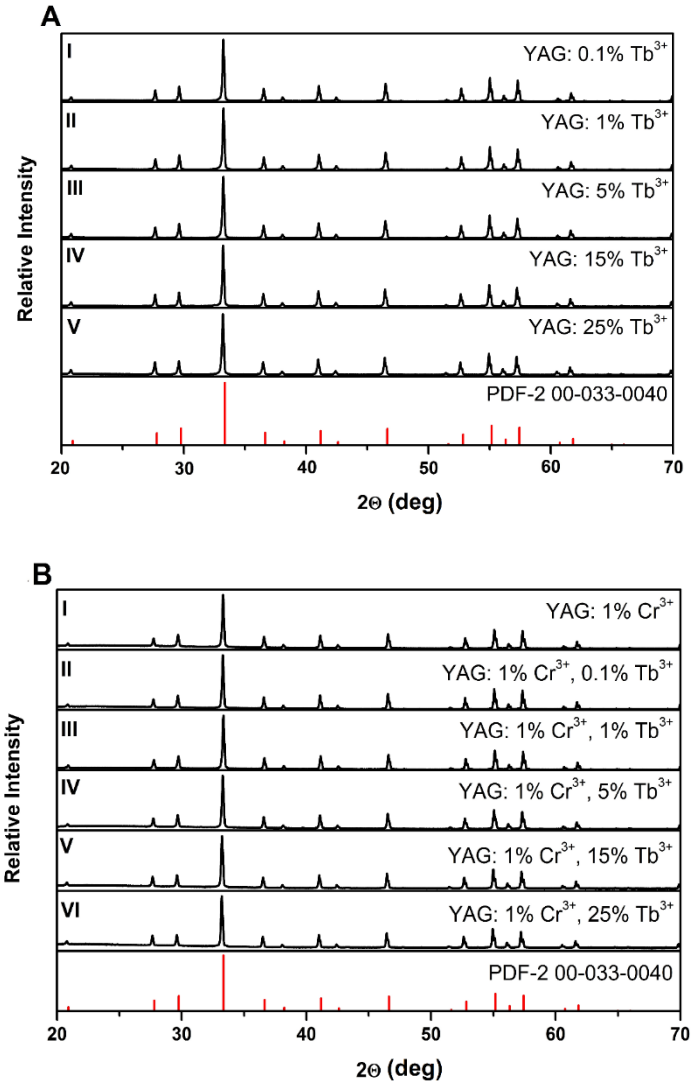

Fig. 24. XRD patterns of YAG:0.1%Tb^{3+} (A-I), YAG:1%Tb^{3+} (A-II), YAG:5%Tb^{3+} (A-III), YAG:15%Tb^{3+} (A-IV), YAG:25%Tb^{3+} (A-V) and YAG:1%Cr^{3+} (B-I), YAG:1%Cr^{3+},0.1%Tb^{3+} (B-II), YAG:1%Cr^{3+},1%Tb^{3+} (B-III), YAG:1%Cr^{3+},5%Tb^{3+} (B-IV), YAG:1%Cr^{3+},15%Tb^{3+} (B-V), YAG:1%Cr^{3+},25%Tb^{3+} (B-VI) sintered at 1500 °C in reducing atmosphere.

The synthesized samples were analyzed by the XRD method. Each observed peak matched the standard XRD data, meaning that all doped and co-doped YAG samples are single phases and possess a cubic garnet crystal structure, corresponding to the space group $Ia\bar{3}d$ (#230). XRD patterns of YAG powders sintered at 1500 °C in reducing atmosphere together with standard XRD data (PDF2 [00-033-0040]) are presented in Figure 24.

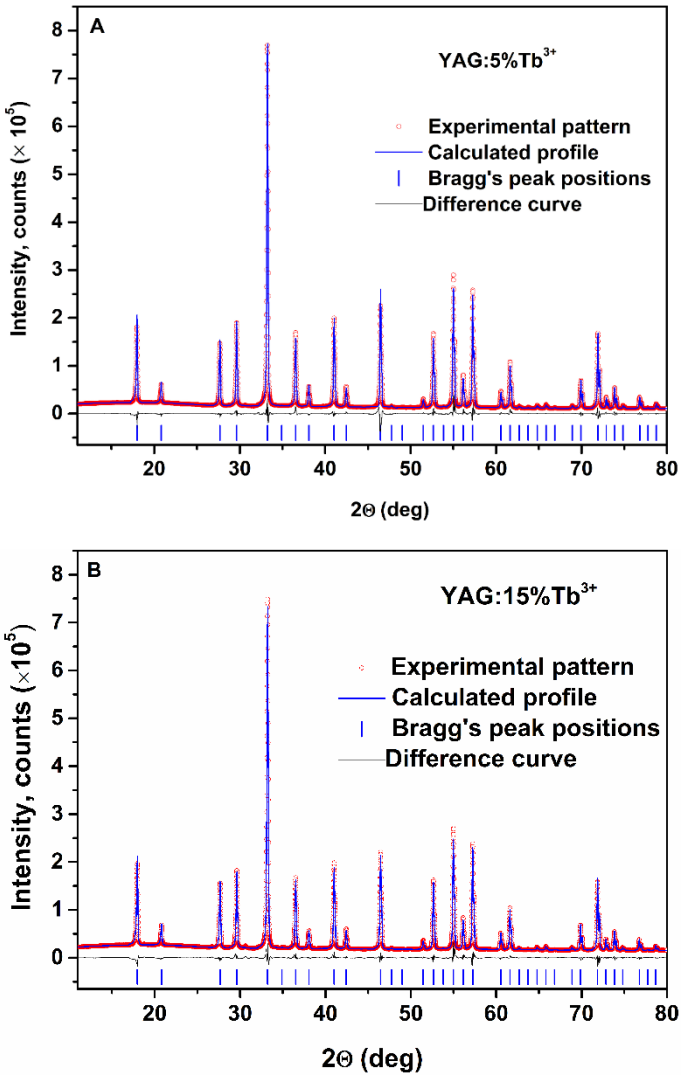

Fig. 25. Rietveld refinement results obtained for YAG:5%Tb^{3+} (A) and YAG:15%Tb^{3+} (B) samples.

Table 4. Crystallographic data for YAG:5%Tb^{3+} and YAG:15%Tb^{3+}.

Atoms, sites	*x/a*	*y/b*	*z/c*	$B_{iso/eq}$, Å^2	Occupancy
YAG:5%Tb^{3+}: *a* = 12.01378(9) Å; R_I = 0.029, R_P = 0.050					
Y/Tb, 24*c*	1/8	0	1/4	1.01(2)	$0.95Y^{3+}$ + $0.05Tb^{3+}$
Al1, 16*a*	0	0	0	0.62(4)	Al^{3+}
Al2, 24*d*	3/8	0	1/4	1.02(3)	Al^{3+}
O, 96*h*	-0.0344(1)	0.0486(1)	0.1494(1)	1.16(4)	O^{2-}
YAG:15%Tb^{3+}: *a* = 12.0190(1) Å; R_I = 0.030, R_P = 0.068					
Y/Tb, 24*c*	1/8	0	1/4	0.79(2)	$0.85Y^{3+}$ + $0.15Tb^{3+}$
Al1, 16*a*	0	0	0	0.80(5)	Al^{3+}
Al2, 24*d*	3/8	0	1/4	0.82(4)	Al^{3+}
O, 96*h*	-0.0343(1)	0.0489(2)	0.1495(2)	0.90(5)	O^{2-}

Moreover, selected samples (YAG:5%Tb^{3+}, YAG:15%Tb^{3+}) were analyzed in more detail by Rietveld refinement technique (Figure 25). The Rietveld analysis also confirmed that there is no evidence of the secondary phases. Figure 26 reveals that the lattice parameters evaluated from XRD long scans (full red diamond symbols) fit well with the PDF-2 data for the pure YAG and TAG garnets and the mixed $(Y_{2/3}Tb_{1/3})_3Al_5O_{12}$ material (full black circles). This also indicates that the dopants were successfully introduced into the garnet matrix.

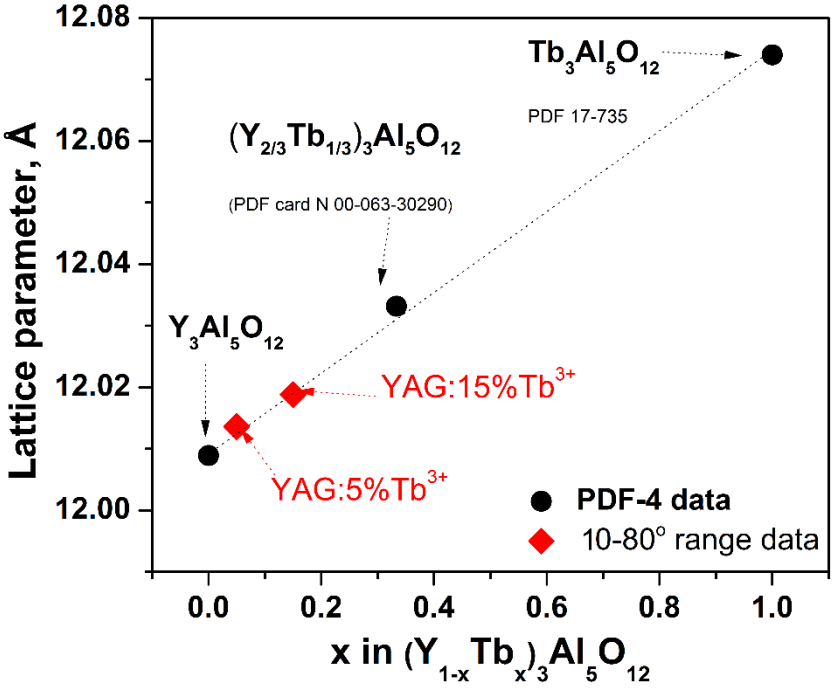

Fig. 26. Concentration dependence of the unit cell parameter *a* in $(Y_{1-x}Tb_x)_3Al_5O_{12}$ series.

3.3.2. Optical properties

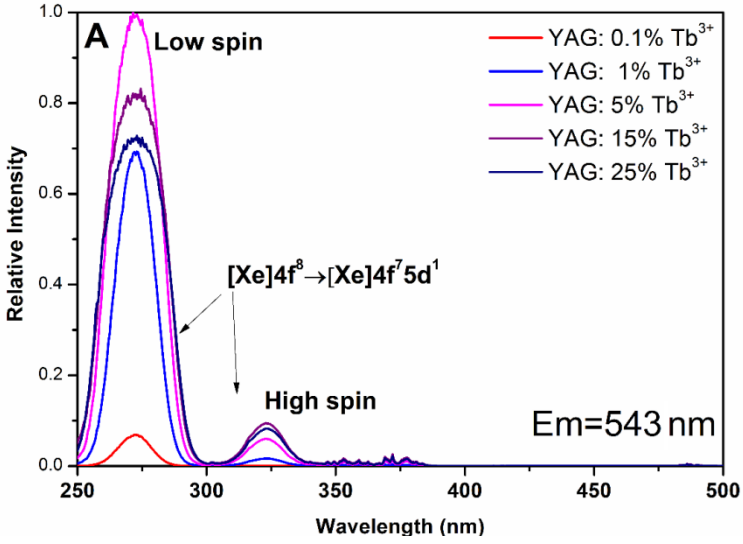

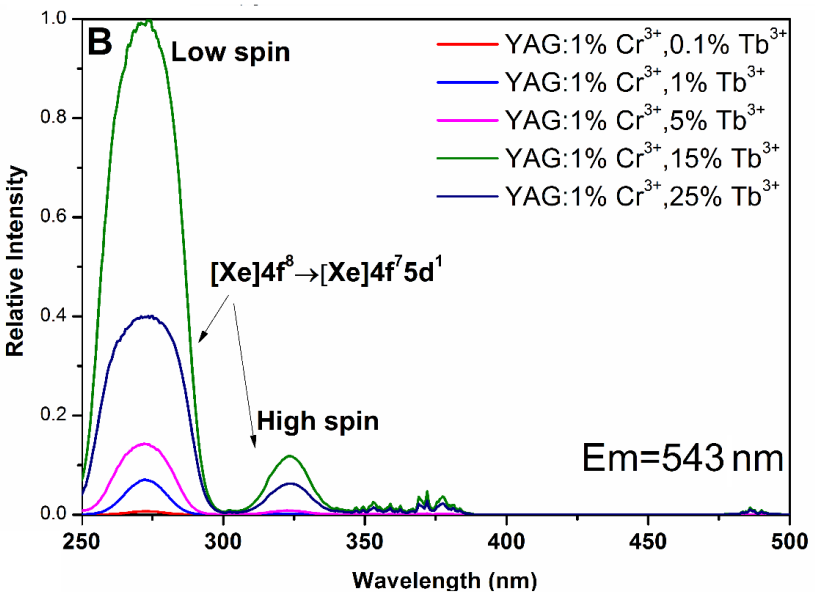

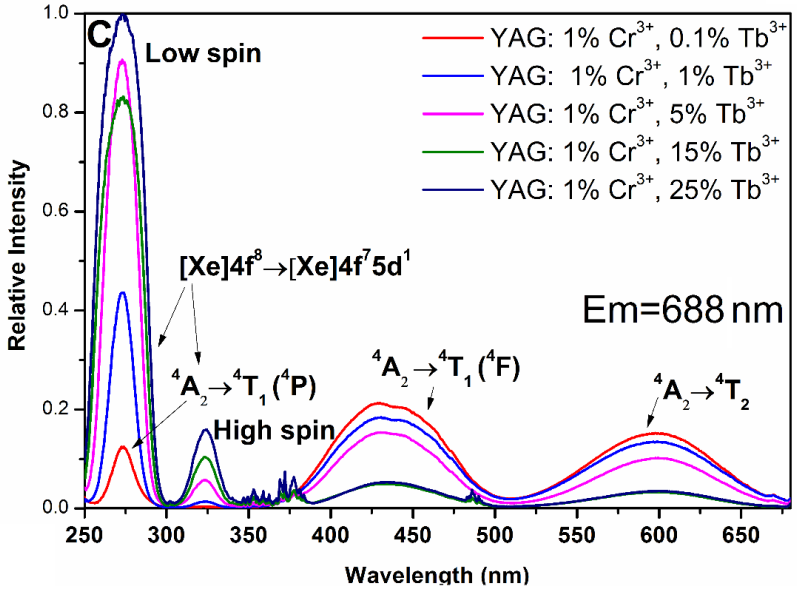

Fig. 27. Excitation spectra of (A) YAG:Tb^{3+} (λ_{em} = 543 nm), (B) YAG:1%Cr^{3+},Tb^{3+} (λ_{em} = 543 nm), and (C) YAG:1%Cr^{3+},Tb^{3+} (λ_{em} = 688 nm).

The excitation spectra of YAG:Tb^{3+} when monitoring emission at 543 nm showed two broad bands from 250 to 300 nm with the maximum at 273 nm,

and from 304 to 343 nm with the maximum at 323 nm. These bands are attributed to the low and high spin transitions [Xe]$4f^8 \rightarrow$[Xe]$4f^7 5d^1$ of Tb^{3+} ions, respectively (Figure 27A). All these transitions of terbium ions are also seen in the data depicted in Figure 27B, where excitation spectra of YAG:1%Cr^{3+},Tb^{3+} are shown. Furthermore, there are excitation lines in Fig. 27A, 27B and 27C in the 345 – 385 nm region attributed to electronic transitions from the $^7F_6$ ground states to $^5L_9$, $^5G_5$, $^5L_{10}$, $^5G_6$ and $^5D_3$ states [21]. There are some changes in excitation spectra of YAG:1%Cr^{3+},Tb^{3+} when emission is monitored for Cr^{3+} emission at 688 nm (Figure 27C) compared to 543 nm emission of Tb^{3+} (Figure 27B). The first two additional broad bands with the maxima ca. 430 and 600 nm appear in Figure 27C. These bands can be assigned to the $^4A_2 \rightarrow {}^4T_1$ (^4F) and $^4A_2 \rightarrow {}^4T_2$ transitions of Cr^{3+} ions, respectively. Another excitation band of Cr^{3+} is observed around 273 nm and is attributed to the $^4A_2 \rightarrow {}^4T_1$ (^4P) transition of Cr^{3+}. However, this band completely overlaps with the low spin [Xe]$4f^8 \rightarrow$[Xe]$4f^7 5d^1$ transition of Tb^{3+} ions. When monitoring Cr^{3+} emission for YAG:1%Cr^{3+},Tb^{3+} samples revealed that energy transfer from Tb^{3+} to Cr^{3+} ions occurs since bands and lines of Tb^{3+} transitions appear in the excitation spectra of Cr^{3+} ions (Figure 23C). It was also concluded that the opposite energy transfer from Cr^{3+} to Tb^{3+} ions does not occur as there were no signs of Cr^{3+} bands in excitation spectra monitored for Tb^{3+} emission (Figure 27B). To conclude, the $Tb^{3+} \rightarrow Cr^{3+}$ energy transfer makes it possible to significantly expand the excitation range of YAG:1%Cr^{3+},Tb^{3+} phosphors.

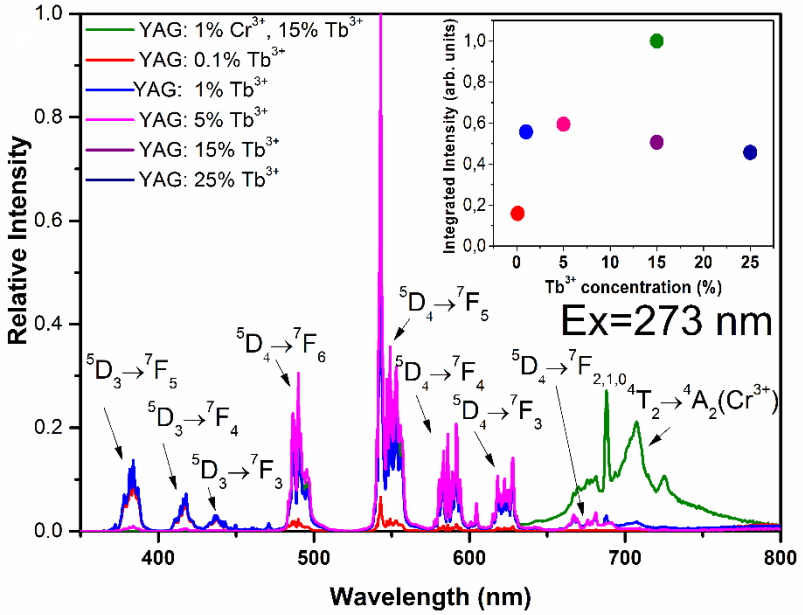

Fig. 28. Emission spectra (λ_{ex} = 273 nm) of YAG:1%Cr^{3+},15%Tb^{3+}, and YAG:Tb^{3+}.

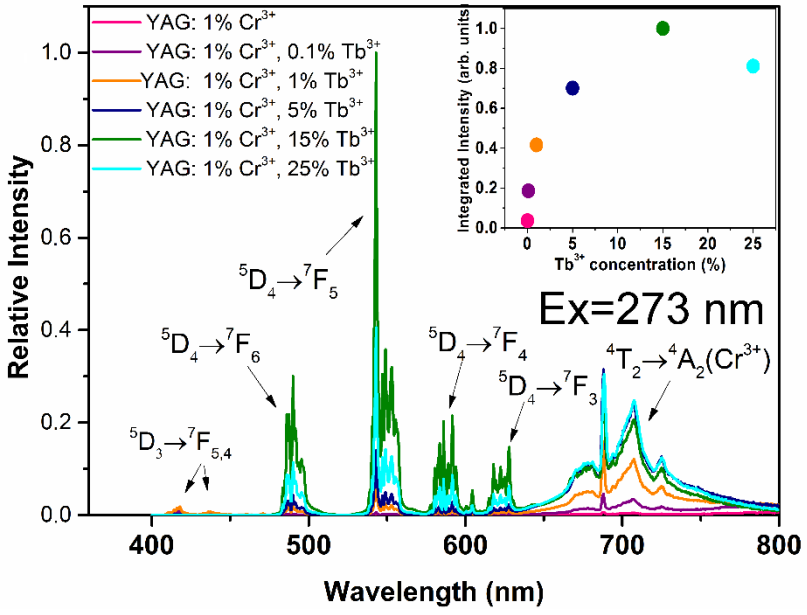

Fig. 29. Emission spectra (λ_{ex} = 273 nm) of YAG:1%Cr^{3+} and YAG:1%Cr^{3+},Tb^{3+}.

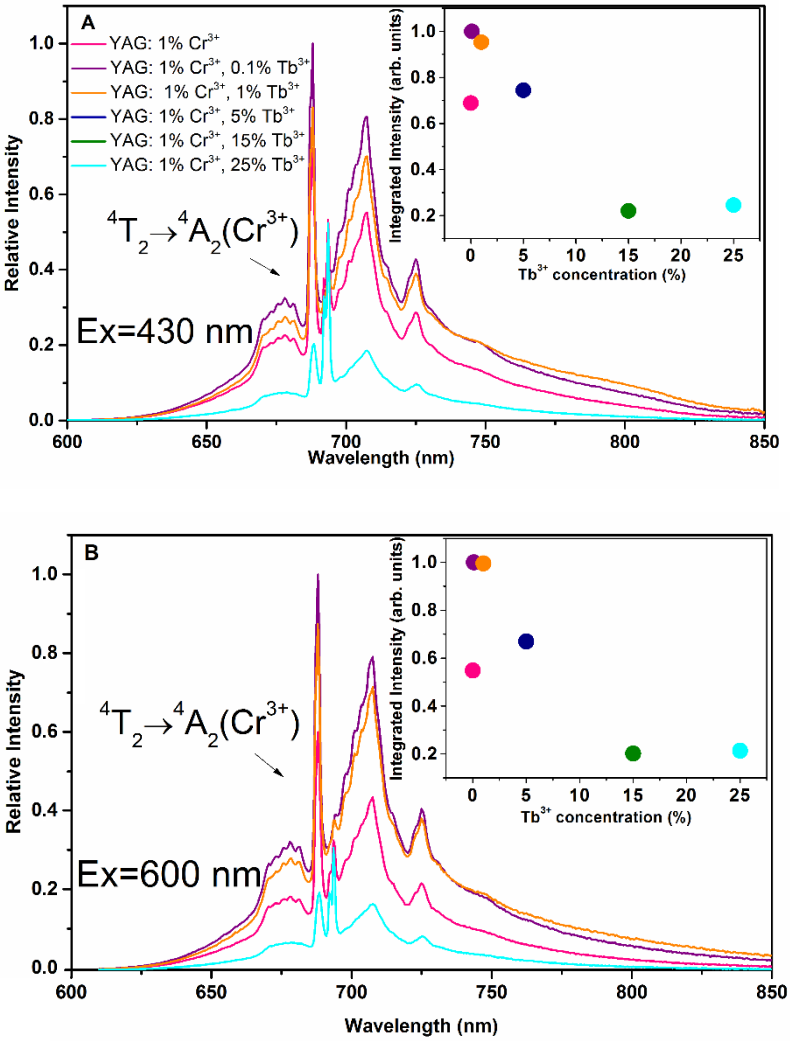

Fig. 30. Emission spectra of YAG:1%Cr^{3+} and YAG:1%Cr^{3+},Tb^{3+} under excitation at (A) 430 nm and (B) 600 nm.

The emission results go hand in hand with the results of excitation spectra. The emission spectra of YAG:Tb^{3+} excited at 273 nm are depicted in Figure 28. All terbium doped garnets exhibit peaks corresponding to $^5D_3 \rightarrow {}^7F_J$ and $^5D_4 \rightarrow {}^7F_J$ transitions. Increasing the concentration of Tb^{3+} leads to decreasing and eventually disappearing emission lines from $^5D_3$ excited level. This process can be described by an electric dipole-dipole interaction and

reduction of efficiency of the multiphonon quenching from the $^5D_3$ state into the $^5D_4$ state [126, 127]. The $^5D_4 \rightarrow {}^7F_5$ transition belonging to Tb^{3+} results in the most intensive emission peak in YAG:5%Tb^{3+}. However, further increasing Tb^{3+} concentration causes a decrease of the intensity of all transitions due to concentration quenching.

Emission spectra of YAG:1%Cr^{3+},Tb^{3+} samples excited at 273 nm are presented in Figure 29. The transitions originating from the $^5D_3$ excited state of terbium ions are visible for the samples co-doped with 0.1%, 1% and 5% of Tb^{3+} ions, meanwhile, transitions from the $^5D_4$ excited state are characteristic for all samples. The emission intensity of the most expressed transitions of YAG:1%Cr^{3+},15%Tb^{3+} sample is 1.2 times lower than the emission intensity of YAG:5%Tb^{3+}. Further increase of the Tb^{3+} concentration leads to noticeable emission quenching. Nevertheless, co-doping with chromium and terbium leads to the expansion of the emission region from 400 nm to more than 800 nm wavelength (additional 200 nm emission range). This additional emission caused by the $^4T_2 \rightarrow {}^4A_2$ transitions corresponds to Cr^{3+} ions and is observed for each compound. The YAG:1%Cr^{3+},15%Tb^{3+} sample exhibits the most intensive emission of chromium ions.

All co-doped phosphors excited by 430 or 600 nm radiation possess a wide emission band at 620-800 nm, which is attributed to $^4T_2 \rightarrow {}^4A_2$ transition of Cr^{3+} ions (Figure 30A and 30B, respectively). The phosphors containing 0.1% or 1% of Tb^{3+} exhibit the highest emission intensity, thus, co-doping with a small amount of terbium strengthens chromium luminescence properties. The explanation could be that terbium ion concentration is low, and the intervals between terbium ions is too large in the lattice so that the energy migration is hampered and concentration quenching is not happening [112].

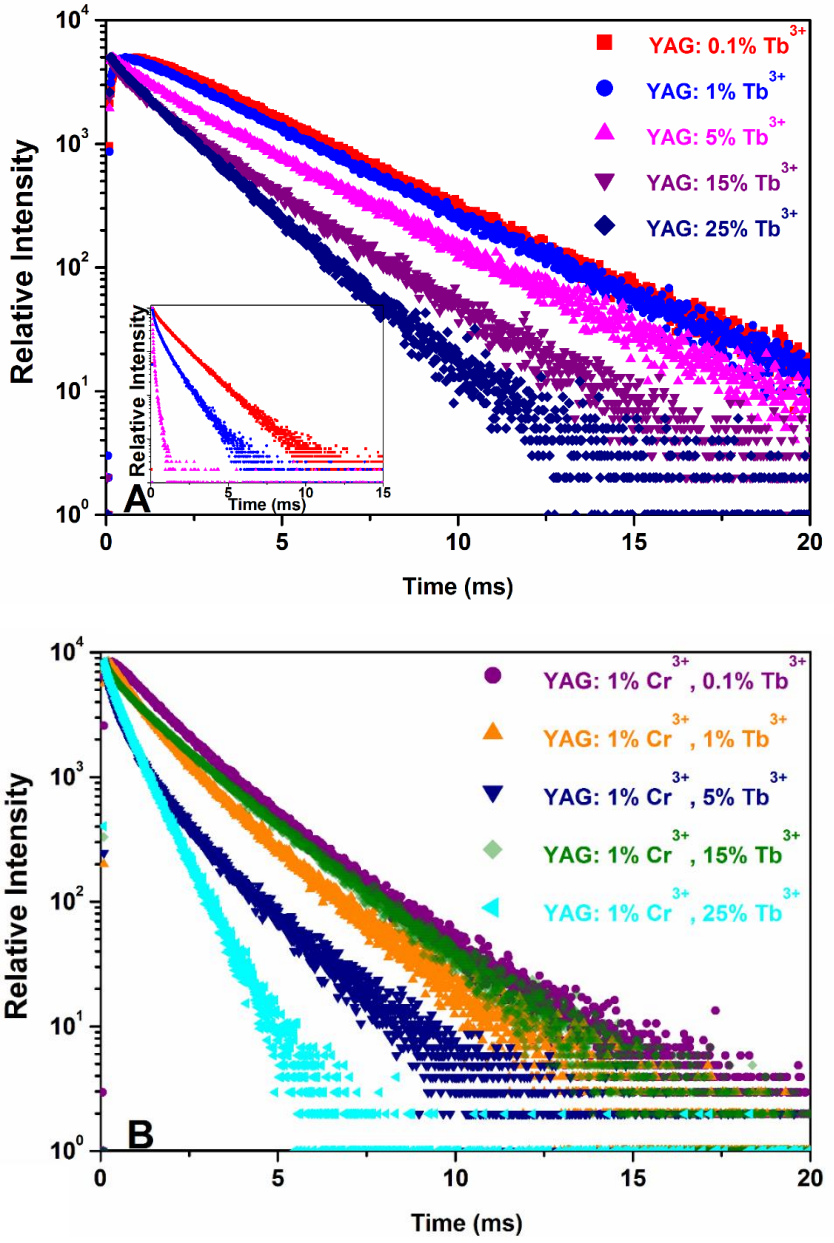

Fig. 31. Photoluminescence decay curves of YAG Tb^{3+} (λ_{ex}=273 nm, λ_{em}=543 nm) (A); and YAG:1%Cr^{3+},Tb^{3+} (λ_{ex}=273 nm, λ_{em}=543 nm) (B). Inset of section A shows PL decay curves for $^5D_3 \rightarrow {}^7F_6$ transition of YAG:Tb^{3+} samples doped with 0.1%, 1% and 5% Tb^{3+} ions (λ_{ex}=273 nm, λ_{em}=384 nm).

Table 5. Calculated PL decay times of YAG:xTb^{3+} and YAG:1%Cr^{3+},xTb^{3+} phosphors (λ_{ex}=273 nm, λ_{em}=543 nm).

Sample	**τ_1, ms**	**τ_1, %**	**τ_2, ms**	**τ_2, %**	**$\tau_{average}$**
1. YAG:0.1%Tb^{3+}	2.6	39	3.5	61	3.1
2. YAG:1%Tb^{3+}	3.0	90	4.2	10	3.1
3. YAG:5%Tb^{3+}	1.1	11	3.0	89	2.8
4. YAG:15%Tb^{3+}	1,0	16	2.4	84	2.2
5. YAG:25%Tb^{3+}	0.5	13	1.4	87	1.3
6. YAG:1%Cr^{3+},0.1%Tb^{3+}	1.3	60	2.3	40	1.7
7. YAG:1%Cr^{3+},1%Tb^{3+}	0.8	45	1.9	55	1.4
8. YAG:1%Cr^{3+},5%Tb^{3+}	0.4	36	1.5	64	1.1
9. YAG:1%Cr^{3+},15%Tb^{3+}	0.7	17	1.9	83	1.7
10. YAG:1%Cr^{3+},25%Tb^{3+}	0.3	17	0.7	83	0.7

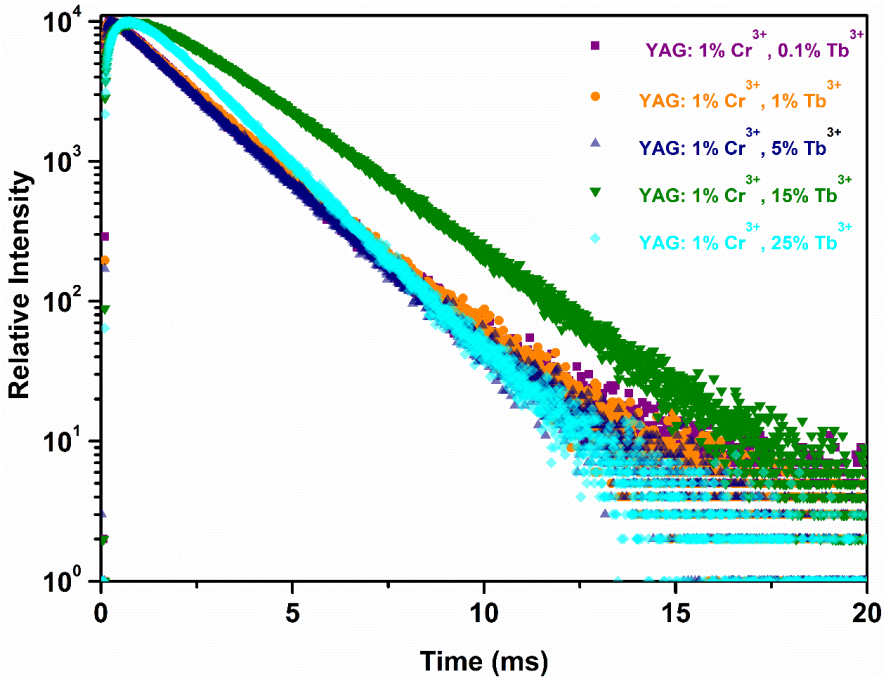

Fig. 32. PL decay curves of YAG:1%Cr^{3+},Tb^{3+} (λ_{ex}=273 nm, λ_{em}=688 nm).

Table 6. Calculated PL decay times of YAG:1%Cr^{3+},Tb^{3+} (λ_{ex}=273 nm, λ_{em}=688 nm).

Sample	**τ_1,ms**	**τ_1, %**	**τ_2,ms**	**τ_2, %**	**$\tau_{average}$**
1. YAG:1% Cr^{3+},0.1%Tb^{3+}	1.7	97	4.8	3	1.8
2. YAG:1% Cr^{3+},1%Tb^{3+}	1.8	93	2.8	7	1.9
3. YAG:1% Cr^{3+},5%Tb^{3+}	1.6	88	2.6	12	1.8
4. YAG:1% Cr^{3+},15%Tb^{3+}	2.2	100	-	-	2.2
5. YAG:1% Cr^{3+},25%Tb^{3+}	1.6	100	-	-	1.6

Table 7. Calculated PL decay times of YAG:1%Cr^{3+},Tb^{3+} (λ_{ex}=600 nm, λ_{em}=688 nm).

Sample	**τ_1,ms**	**τ_1, %**	**τ_2,ms**	**τ_2, %**	**$\tau_{average}$**
1. YAG:1% Cr^{3+}	0.7	13	1.8	87	1.6
2. YAG:1% Cr^{3+},0.1%Tb^{3+}	0.6	11	1.8	89	1.6
3. YAG:1% Cr^{3+},1%Tb^{3+}	0.5	12	1.8	88	1.6
4. YAG:1% Cr^{3+},5%Tb^{3+}	0.6	13	1.7	87	1.5
5. YAG:1% Cr^{3+},15%Tb^{3+}	1.1	19	1.8	81	1.7
6. YAG:1% Cr^{3+},25%Tb^{3+}	0.9	22	1.6	78	1.5

Luminescence properties were further investigated by measuring the photoluminescence decay curves of (co-)doped garnets. All YAG compounds doped with Tb^{3+} ions (Figure 31A) exhibit bi-exponential photoluminescence decay. Bi-exponential lifetime indicates that there should be two different depopulation mechanisms of Tb^{3+} excited states. The measured PL decay curves become steeper with increasing Tb^{3+} concentration indicating that the lifetime of excited state becomes shorter. This is supported by the calculated PL lifetime values which are given in Table 5. Besides, it is also interesting to note that samples doped with rather low Tb^{3+} concentrations possess a significant rise in decay time. The increased decay time is a phenomenon which can be observed in the decay curve if the emission intensity increases for a period of time after excitation is stopped. The increment of the emission

intensity is related to the increment of the number of the excited activator ions over time [137]. In our case, the PL decay curves were measured for the $^5D_4 \rightarrow {}^7F_5$ transition. The observed decay time rise means that the emitting $^5D_4$ state must be additionally populated after the excitation pulse is cut off. It is most likely that this additional population of $^5D_4$ states is caused by non-radiative relaxation from $^5D_3$ states, from which the strongest emission (see Figure 28) at low Tb^{3+} concentrations (0.1% and 1%) is also observed. This assumption is supported by the fact that the PL decay curves of $^5D_3 \rightarrow {}^7F_6$ transition (see inset of Figure 31A) are roughly in the same range as measured for the $^5D_4 \rightarrow {}^7F_5$ transition. The calculated rise in decay time of YAG:0.1%Tb^{3+} and YAG:1%Tb^{3+} samples ($^5D_4 \rightarrow {}^7F_5$ transition) is 0.55 and 0.34 ms, respectively, whereas the average PL lifetime values of $^5D_3 \rightarrow {}^7F_6$ transition for the same sample are 1.17 and 0.62 ms, respectively, i.e., the excited $^5D_3$ state exists long enough to populate the $^5D_4$ states to some extent. Furthermore, the PL lifetime of $^5D_3 \rightarrow {}^7F_6$ transition in YAG:5%Tb^{3+} is only 0.08 ms and, therefore, the decay rise time for $^5D_4 \rightarrow {}^7F_5$ transition in this sample is no longer observed. The decrease of PL lifetime values over the increase of Tb^{3+} concentration can be associated with the increasing rate of cross-relaxation processes, which can be expressed by the following equation [116]:

$$Tb^{3+}\ (^5D_3) + Tb^{3+}\ (^7F_6) \rightarrow Tb^{3+}\ (^5D_4) + Tb^{3+}\ (^7F_0) \qquad \text{(Eq. 2.)}$$

The PL decay curves for $^5D_4 \rightarrow {}^7F_5$ transition of YAG:1%Cr^{3+},Tb^{3+} samples (Figure 31B) are steeper than their YAG:Tb^{3+} counterparts. This shows that the average lifetime value of $^5D_4$ excited state is also shorter as Tb^{3+} concentration increases, i.e., ~1.7 ms, ~1.4 ms, ~1.0 ms, ~1.7 ms and ~0.7 ms for YAG:1%Cr^{3+},Tb^{3+} samples co-doped with 0.1%, 1%, 5%, 15%, 25% of Tb^{3+} ions, respectively. It should be noted that the lifetime data of ~1.7 ms for the Tb^{3+} co-doped sample with 15% does not obey the simply shortening rule and, unfortunately, the explanation for this exception could not be found in the literature. The reduction of lifetime values, except the Tb^{3+} co-doped sample with 15%, can be attributed to the occurring $Tb^{3+} \rightarrow Cr^{3+}$ energy transfer, which opens additional channel for $^5D_4$ state depopulation.

Figure 32 demonstrates that co-doping YAG:1%Cr^{3+} with terbium ions from 0.1% to 5% caused a slight decrement of the lifetime ($\tau_{average}$) values of the phosphor from ~1.8 ms to ~1.7 ms. It is noteworthy that the decay time rise of YAG:1%Cr^{3+},15%Tb^{3+} and YAG:1%Cr^{3+},25%Tb^{3+} compounds increases significantly (see Fig. 32). The shape of the decay lifetime illustrates

the ion-ion (Tb-Tb) interactions [117-119]. YAG:1%Cr^{3+},15%Tb^{3+}, YAG:1%Cr^{3+},25%Tb^{3+} lifetime ($\tau_{average}$) value is ~2.2 ms and 1.6 ms, respectively. The photoluminescence of the latter two samples follows the single-exponential decay. It should be mentioned that the parameter τ_1 is dominating if the lifetime is measured for the compounds excited by λ_{ex}=273 nm and emission recorded for λ_{em}=688 nm, caused by the transitions from the $^5D_4$ excited state, which are dominating [15, 120]. The persistent increase of the counts after the excitation source is stopped might illustrate the energy transfer from terbium ions to chromium ions. The detailed mechanism is discused in reference [121]. The more efficient energy transfer probably causes the more delayed saturation. Besides, the lifetime of co-doped YAG (λ_{ex}=600 nm, λ_{em}=688 nm) varies inconsistently (Table 7). Highest lifetime values attributed to YAG:1%Cr^{3+},15%Tb^{3+}, however the values of the lifetime themselves change only slightly. The average lifetime approximately changes from ~1.6 ms to ~1.4 ms, since chromium concentration is constant. In addition, the τ_1 value is low meaning the process is very quick [122, 123]. Nevertheless, the τ_2 (Table 7) and τ_1 (Table 6) values are comparable caused by Cr^{3+} transitions (λ_{ex} and λ_{em} are characteristic for chromium ions). Table 6 also provides information about Cr^{3+} transitions, however, λ_{ex} value is 273nm (characteristic for Tb^{3+}), consequently, (Table 6.) values can be influenced not only by Cr^{3+}, but also by Tb^{3+} transitions.

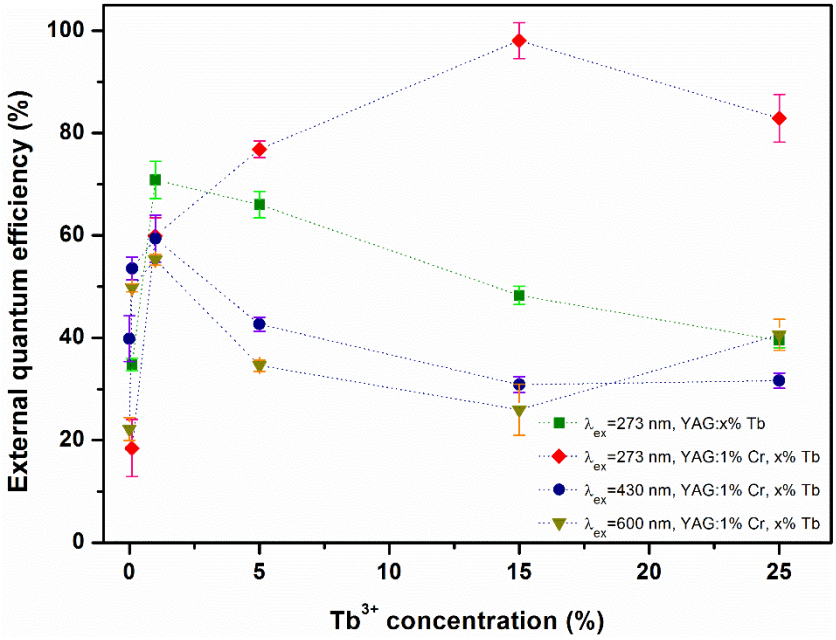

Fig. 33. External quantum efficiencies of (co-)doped YAG phosphors as a function of Tb^{3+} concentration and excitation wavelength. The lines are drawn to guide the eye.

The calculated EQE for co-doped YAG phosphors under three excitation wavelengths are depicted in Figure 33. The maximum value of EQE is 98% for YAG:1%Cr^{3+},15% Tb^{3+} under 273 nm excitation. The better EQE of chromium or terbium doped or chromium and terbium co-doped compound was not reported in the literature to the best of our knowledge. Further increasing of the concentration of terbium ions leads to the decrease of EQE of the phosphor. Again, this might be caused by the concentration quenching. If a compound is doped only with terbium ions, the maximum of EQE is 70% for YAG:1%Tb^{3+}.

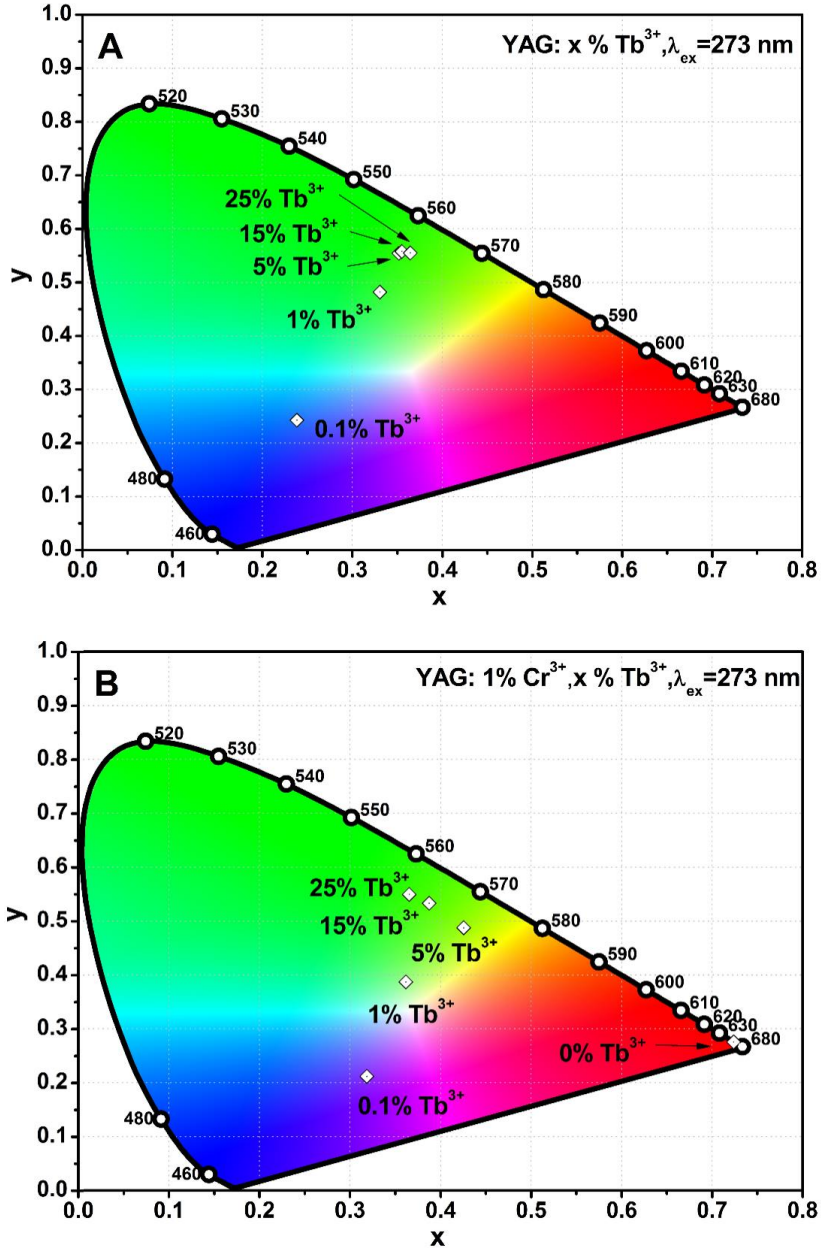

Fig. 34. CIE 1931 color space diagram combined with the color coordinates of terbium ions doped YAG (A) and terbium ions co-doped YAG:1%Cr^{3+} (B).

Figure 34 shows the color coordinates of doped (Figure 34A) and co-doped (Figure 34B) YAG phosphors. YAG:0.1%Tb^{3+} color coordinates are in the

blue region of the CIE 1391 color space diagram, whereas color coordinates of YAG:1%Tb^{3+}, YAG:5%Tb^{3+}, YAG:15%Tb^{3+}, and YAG:25%Tb^{3+} samples are in the green region (Figure 34A). This is consistent with the emission spectra of YAG:1%-25%Tb^{3+} samples shown in Figure 28. The color coordinate of YAG:1%Cr^{3+}, in turn, lies in the deep red region (Figure 34B). Co-doping YAG:1%Cr^{3+} with 0.1%Tb^{3+} shifted to red into the blue-purple region due to the mixing of red Cr^{3+} emission band and blue/green emission lines of Tb^{3+} ions. Increasing the concentration of terbium ions to 1% yields a color coordinate nearly in the white light region due to admixing of blue, green and red emission lines/bands of Tb^{3+} and Cr^{3+} ions present in this sample. As was discussed above, increasing Tb^{3+} concentration to and above 5% leads to an absence of $^5D_3 \rightarrow {}^7F_J$ transition in the violet/blue region thus shifting the color coordinates to green/yellow region of CIE 1931 color space diagram. The given results indicate that co-doping of YAG:1%Cr^{3+} with Tb^{3+} ions provides the opportunity to simulate emission colors to some extent.

CONCLUSIONS

1. All single phase doped and co-doped yttrium aluminum garnet samples were synthesized via citric acid sol-gel route. The thermal analysis of the doped and co-doped YAG showed, that there is no mass changes as temperature is raised above ~800 °C.

2. It was demonstrated, that doping and co-doping (YAG:5%Tb^{3+}, YAG:4.8%Cr^{3+}, YAG:4.8%Cr^{3+},5%Tb^{3+}) does not affect the morphology of synthesized samples. Powder contain the micro-size agglomerates with well-shaped irregular sphere-like particles.

3. All doped and co-doped YAG samples, excited by 430 or 600 nm radiation possess a wide emission band at 620 – 800 nm, which is attributed to $^2E \rightarrow {}^4A_2$ transition of Cr^{3+} ions. It was found that doping or co-doping YAG, the optimal concentration of Cr^{3+} ions is 1%.

4. YAG:*x*Tb^{3+} samples, excited at 273 nm, exhibit peaks corresponding to $^5D_3 \rightarrow {}^7F_J$ and $^5D_4 \rightarrow {}^7F_J$ transitions. The transitions originating from the $^5D_3$ excited state of Tb^{3+} are visible for the samples with the lower concentration of Tb^{3+} ions $x = 0.1\%$ and 1%. Increasing the concentration of Tb^{3+} leads to decreasing and eventually disappearing emission lines from $^5D_3$ excited level. The $^5D_4 \rightarrow {}^7F_5$ transition belonging to Tb^{3+} result in the most intensive emission peak in YAG:5%Tb^{3+}. Further, increasing Tb^{3+} concentration causes a decrease of the intensity of all transitions due to concentration quenching.

5. Co-doped samples of YAG:1%Cr^{3+},*x*Tb^{3+} excited at 273 nm. The transitions originating from the $^5D_3$ excited state of terbium ions are visible for the samples co-doped when $x = 0.1\%$, 1% and 5% of Tb^{3+} ions. Meanwhile, transitions from the $^5D_4$ excited state are dominating for all samples.

6. All co-substituted phosphors excited by 430 or 600 nm radiation possess a wide emission band at 620 – 800 nm, which is attributed to $^2E \rightarrow {}^4A_2$ transition of Cr^{3+} ions. The phosphors containing even small amount of terbium strengthens chromium luminescence properties.

7. The maximum value of calculated external quantum efficiency for doped and co-doped YAG phosphors the EQE is 98% for YAG:1%Cr^{3+},15% Tb^{3+} under 273 nm excitation. When yttrium aluminum garnet is doped only by terbium ions, the maximum of EQE is 70% for YAG:1%Tb^{3+}.

8. Co-doping YAG:1%Cr^{3+} with 0.1%Tb^{3+} shifted to red into the blue-purple region. Increasing the concentration of terbium ions to 1 % yields a color coordinate nearly in the white light region. YAG:1% Cr^{3+} doped from 5 %to 25 % is shifted from green to yellowish-green light region. The given results indicate that co-doping of YAG:1%Cr^{3+} with Tb^{3+} ions provides the opportunity to simulate emission colors to some extent.

9. The aforementioned optical properties indicates that YAG:Cr^{3+},Tb^{3+} can be promising potential candidates not only for solid-state lighting but for the application in near UV light emitting diodes.

ACKNOWLEDGEMENTS

Although my name is on the cover of this thesis, many people were of great importance for this research. I would like to take a moment to extend my gratitude to the involved.

First of all, I would like to thank Prof. Aivaras Kareiva and all the team of Sol-Gel Chemistry Group, not only for practically helping, but also for their valued opinions, explanations, and the atmosphere, it made me enjoy every second of working in Sol-Gel Group and on my thesis.

I would like to give a special mention to a special person, my supervisor, Assoc. Prof. Dr. Ramunas Skaudzius, without whom this dissertation would probably have ended at page 2. Many thanks to You, for not only guiding me in practically every step of the research but also for your efforts to make me feel like home while working.

I would like to thank Assoc. Prof. Dr. Arturas Katelnikovas for his friendly approach, guiding hand and valuable remarks.

Lastly, I want to mention my family, my beloved husband Giedrius, my beautiful daughter Aja and my Mom and Dad. Thank You, for making me the person that I have become, for your huge patience and support. The true aim of this dissertation is to make the four of you proud, and I hope I had succeeded at this goal.

Once I promised to myself, to dedicate this final work, of my PhD studies, to my brother Vincas, and this might be the right moment to do so. I know You see me and I still miss You dearly every day.

REFERENCES

1. Dong, L. M., et al., Synthesis of Green-Emitting Phosphor $Y_3Al_5O_{12}$: Tb, Ce, Gd by Sol-Gel Method, High-Performance Ceramics IV, 336-338 (2007) 610-612.
2. Solodovnikov, D., et al., Improvement in Scintillation Performance of Ce, Er Codoped Yttrium Aluminum Garnet Crystals by Means of a Postgrowth Treatment, Applied Physics Letters, 93(10) (2008) 104102.
3. Ghrib, T., et al., Structural, Optical and Thermal Properties of the Ce Doped YAG Synthesized by Solid State Reaction Method, Thermochimica Acta, 654 (2017) 35-39.
4. Gong, C., et al., Synthesis and Characterization of Structural and Optical Properties of Ce, U Codoped YAG Transparent Ceramics, Optical Materials Express, 8(5) (2018) 1274-1281.
5. Xia, G. D., et al., Structural and Optical Properties of YAG : Ce^{3+} Phosphors By Sol-Gel Combustion Method, Journal of Crystal Growth, 279(3-4) (2005) 357-362.
6. Chen, M. T., et al., Near UV LEDs Made With in situ Doped Pn Homojunction ZnO nanowire arrays, Nano letters, 10(11) (2010) 4387-4393.
7. Huang, C. H., et al., (Ca, Mg, Sr) $_9$ Y (PO $_4$) $_7$: Eu $^{2+}$, Mn $^{2+}$: Phosphors for white-light near-UV LEDs Through Crystal Field Tuning And Energy Transfer, Journal of Materials Chemistry, 21(28) (2011) 10489-10495.
8. Hirayama, H., et al., 222–282 nm AlGaN and InAlGaN-Based Deep-UV LEDs Fabricated on High-Quality AlN on Sapphire, Physica Status Solidi (a), 206(6) (2009) 1176-1182.
9. Siegel, S. B., Light Emitting Apparatus and Method for Curing Inks, Coatings and Adhesives. 2007, Google Patents.10. Siegel, S.B., *UV printing and curing of CDs, DVDs, Golf Balls And Other Products*. 2009, Google Patents.
10. Siegel, S.B., UV Printing and Curing of CDs, DVDs, Golf Balls And Other Products. 2009, Google Patents.
11. Song, K., et al., Application of Ultraviolet Light-Emitting Diodes (UV-LEDs) for Water Disinfection: A Review. Water Research, 94 (2016) 341-349.
12. Kneissl, M., et al., Advances in Group III-Nitride-Based Deep UV Light-Emitting Diode Technology, Semiconductor Science and Technology, 26(1) (2010) 014036.
13. Akasaki, I., Nobel Lecture: Fascinated Journeys Into Blue Light, Reviews Of Modern Physics, 87(4) (2015) 1119-1131.
14. Nakamura, S., et al., Candela-Class High-Brightness Ingan/Algan Double-Heterostructure Blue-Light-Emitting Diodes, Applied Physics Letters, 64(13) (1994) 1687-1689.

15. Chang-Kui D., et al., $^5D_3$–$^5D_4$ Cross-Relaxation of Tb^{3+} in a Cubic Host Lattice, Chemical Physics Letters, 506 (2011) 179-182.
16. Wang, L., et al., Interionic Energy Transfer in $Y_3Al_5O_{12}$: Ce^{3+}, Pr^{3+}, Cr^{3+} Phosphor, Journal of the Electrochemical Society, 159(4) (2012) F68-F72.
17. Pereira, P. F. S., et al., Red, Green and Blue (RGB) Emission Doped $Y_3Al_5O_{12}$ (YAG) Phosphors Prepared by Non-Hydrolytic Sol-Gel Route, Journal of Luminescence, 130(3) (2010) 488-493.
18. Gluchowski, P., et al., Luminescence Properties of Cr^{3+}:$Y_3Al_5O_{12}$ Nanocrystals, Journal of Luminescence, 129(5) (2009) 548-553.
19. Bachmann, V., et al., Temperature Quenching of Yellow Ce^{3+} Luminescence in YAG:Ce, Chemistry of Materials, 21(10) (2009) 2077-2084.
20. Fu, Y.P., et al., Preparation of $Y_3Al_5O_{12}$: Cr Powders by Microwave-Induced Combustion Process And Their Luminescent Properties, Journal of Alloys and Compounds, 395(1-2) (2005) 227-230.
21. Guo, X.Z., et al., Phase Evolution of Yttrium Aluminium Garnet (YAG) in a Citrate-Nitrate Gel Combustion Process, Journal of Materials Chemistry, 14(8) (2004) 1288-1292.
22. Hreniak, D., et al., Luminescence Properties of Tb^{3+}: $Y_3Al_5O_{12}$ Nanocrystallites Prepared by the sol-gel Method, Optical Materials, 26(2) (2004) 117-121.
23. Chen, Y., et al., High Efficient and Low Color-Temperature White Light-Emitting Diodes with $Tb_3Al_5O_{12}$: Ce^{3+} Phosphor, Applied Physics Letters, 91(7) (2007) 071117.
24. Hansen, P., et al., Magnetic and Magneto-Optical Properties of Garnet Films, Thin solid films, 114(1-2) (1984) 69-107.
25. Hansen, P., et al., Magnetic and Magneto-Optic Properties of Lead-And Bismuth-Substituted Yttrium Iron Garnet Films, Physical Review B, 27(11) (1983) 6608.
26. Sartini, L., et al., Nuclear Instruments and Methods in Physics Research Section a: Accelerators, Spectrometers, Detectors and Associated Equipment, Nuclear Instruments and Methods in Physics Research A, 2010.
27. Chenais, S., et al., Diode-Pumped Yb: GGG Laser: Comparison With Yb: YAG, Optical Materials, 22(2) (2003) 99-106.
28. Slack, G. A., et al., Thermal Conductivity of Garnets and Phonon Scattering by Rare-Earth Ions, Physical Review B, 4(2) (1971) 592.
29. Ronda, C. R., et al., Rare Earth Phosphors: Fundamentals And Applications, Journal of Alloys and Compounds, 275 (1998) 669-676.
30. L. Pavasaryte, et al., Eu^{3+}-Doped $Y_{3x}Nd_xAl_3O_{12}$ Garnet: Synthesis And Structural Investigation, Royal Society of Chemistry, 19 (2017) 3729-3737.

31. Setlur, A. A., et al., Crystal Chemistry and Luminescence of Ce^{3+}-Doped ($LuCaMg_2$)-Ca-$_2$(Si, Ge)($_3$)O_{12} and its Use in LED Based Lighting, Chemistry of Materials, 18(14) (2006) 3314-3322.
32. Guo, K., et al., Comparative Study on Photoluminescence of Amorphous and Nano-Crystalline YAG: Tb Phosphors Prepared by a Combustion Method, Journal of Non-Crystalline Solids, 358(1) (2012) 88-92.
33. Geiger, C. A., Garnet: A Key Phase in Nature, the Laboratory, and Technology, Elements, 9(6) (2013) 447-452.
34. Ozen, G., et al., Effect of Spatial Confinement on Luminescence of $Y_3Al_5O_{12}$ Nano-Particles Doped with Chromium Ions, Journal of Luminescence, 144 (2013) 191-197.
35. Zhu, Q.Q., et al., Synthesis of the High Performance YAG:Ce Phosphor by a Sol-Gel Method, Ecs Journal of Solid State Science and Technology, 1(4) (2012) R119-R122.
36. Nazarov, M., New Generation of Europium-and Terbium-Activated Phosphors: From Syntheses to Applications, Pan Stanford 2011.
37. Hoad, T. F., The Concise Oxford Dictionary of English Etymology, Oxford University Press Oxford 1993.
38. Shackelford, J. F., et al., Ceramic and Glass Materials, JF Shackelford, RH Doremus, 2008.
39. Menzer, G., XX. Die Kristallstruktur der Granate, Zeitschrift für Kristallographie-Crystalline Materials, 69(1-6) (1929) 300-396.
40. Pecharsky, V., et al., Fundamentals of powder diffraction and structural characterization of materials, Springer Science & Business Media (2008).
41. Kuklja, M. M., et al., Atomistic Modeling of Native Point Defects in Yttrium Aluminum Garnet Crystals, Journal of the American Ceramic Society, 82(10) (1999) 2881-2886.
42. Hosokawa, S., et al., Defect Structure of Rare Earth Aluminium Garnets Obtained By The Glycothermal Method, Journal of Alloys and Compounds, 451(1-2) (2008) 309-313.
43. Xu, Y.N. et al., Electronic Structure of Yttrium Aluminum Garnet ($Y_3Al_5O_{12}$), Physical Review B, 59(16) (1999) 10530-10535.
44. Acharyya, S. S., et al., Fabrication of $CuCr_2O_4$ Spinel Nanoparticles: A Potential Catalyst for the Selective Oxidation of Cycloalkanes via Activation of C_{sp3}-H bond, Catalysis Communications, 59 (2015) 145-150.
45. Abel, A., 24 - The History of Dyes and Pigments: From Natural Dyes to High Performance Pigments A2 - Best, J., in Colour Design: Theories and Applications (Second Edition), Woodhead Publishing, (2017) 557-587.

46. Hakuta, Y., et al., Continuous Production of Phosphor YAG : Tb Nanoparticles by Hydrothermal Synthesis in Supercritical Water, Materials Research Bulletin, 38(7) (2003) 1257-1265.
47. Potdevin, A., et al., Luminescent Nanocomposites Made of Finely Dispersed $Y_3Ga_5O_{12}$:Tb Powder in a Polymer Matrix: Promising Candidates for Optical Devices, Langmuir, 28(37) (2012) 13526-13535.
48. Abell, J., et al., An Investigation of Phase Stability in the Y_2O_3-Al_2O_3 System, Journal of Materials Science, 9(4) (1974) 527-537.
49. Tanner, P. A., et al., Preformed Sol-Gel Synthesis and Characterization of Lanthanide Ion-Doped Yttria-Alumina Materials, Physica Status Solidi (A), 199(3) (2003) 403-415.
50. Zabiliute, A., et al., Sol-Gel Synthesized Far-Red Chromium-Doped Garnet Phosphors for Phosphor-Conversion Light-Emitting Diodes That Meet the Photomorphogenetic Needs of Plants, Applied Optics, 53(5) (2014) 907-914.
51. Zhang, J. J., et al., Synthesis of Ultrafine YAG : Tb Phosphor by Nitrate-Citrate Sol-Gel Combustion Process, Materials Research Bulletin, 38(7) (2003) 1249-1256.
52. Pechini, M. P., Method of Preparing Lead and Alkaline Earth Titanates and Niobates and Coating Method Using the Same to Form a Capacitor, U.S.P. Office, Editor, (1967) US.
53. Matsubara, I., et al., Preparation of Cr-doped $Y_3Al_5O_{12}$ Phosphors by Heterogeneous Precipitation Methods and Their Luminescent Properties, Materials Research Bulletin, 35(2) (2000) 217-224.
54. Grinberg, E., et al., Technological Aspects of Preparation of High-Purity Compounds for Sol-Gel and Pyrolytic Synthesis Methods, Glass Physics and Chemistry, 34(4) (2008) 515.
55. Hench, L.L., et al., The sol-gel process, Chemical reviews, 90(1) (1990) 33-72.
56. Belyakov, A., et al., Methods for Synthesizing Yttrium-Aluminum Garnet Nanopowders From Solutions, Refractories and Industrial Ceramics, 52(2) (2011) 155.
57. Dastjerdi, R. et al., A Review on the Application of Inorganic Nano-Structured Materials in the modification of textiles: focus on Anti-Microbial Properties, Colloids and Surfaces B: Biointerfaces, 79(1) (2010) 5-18.
58. Vaqueiro, P., et al., Synthesis of Yttrium Aluminium Garnet by the Citrate Gel Process, Journal of Materials Chemistry, 8(1) (1998) 161-163.
59. Ahmed, I.S., et al., Synthesis and Characterization of New Nano-Particles as Blue Ceramic Pigment, Spectrochimica Acta Part a-Molecular and Biomolecular Spectroscopy, 71(2) (2008) 616-620.

60. Sytschev, A.E., et al., Self-Propagating High-Temperature Synthesis of Nanomaterials, Russian chemical reviews, 73(2) (2004) 147-159.
61. Asakura, R., et al., Effects of Citric Acid Additive on Photoluminescence Properties of YAG: Ce^{3+} Nanoparticles Synthesized by Glycothermal Reaction, Journal of Luminescence, 127(2) (2007) 416-422.
62. Chung, B., Synthesis of Yttrium Aluminium Garnet Powder by a Citrate Gel Method, Journal of Ceramic Processing & Research, 4(3) (2003) 145-150.
63. Loiko, E.M., et al., Studies on Sol-Gel Processes Accompanying Formation of the Yttrium Aluminum Garnet Nanocrystals, Materiały Elektroniczne, 34 (2006) 74-88.
64. Choe, J.Y., et al., Alkoxy Sol-Gel Derived $Y_{3-x} Al_5 O_{12}$: Tb_x Thin Films as Efficient Cathodoluminescent Phosphors, Applied Physics Letters, 78(24) (2001) 3800-3802.
65. Zhang, Q., et al., Influence of Annealing Atmosphere and Temperature on Photoluminescence of Tb^{3+} Or Eu^{3+}-Activated Zinc Silicate Thin Film Phosphors Via Sol–Gel Method, Chemical Physics Letters, 351(3-4) (2002) 163-170.
66. Pereira, P.F., et al., Microwave Synthesis of YAG: Eu by sol–gel Methodology, Journal of Luminescence, 126(2) (2007) 378-382.
67. Rabinovitch, Y., et al., Freeze-Dried Nanometric Neodymium-Doped YAG Powders for Transparent Ceramics, Journal of Materials processing technology, 199(1-3) (2008) 314-320.
68. Cone, R., et al., Rare-Earth-Doped Materials with Application to Optical Signal Processing, Quantum Information Science, and Medical Imaging Technology, in Advances in Photonics of Quantum Computing, Memory, and Communication V. International Society for Optics and Photonics (2012).
69. Lorgeré, I., et al., Radio-Frequency Spectrum Analyzers Based on Rare Earth Ion Doped Crystals, Applied Physics B, 84(4) (2006) 653-657.
70. Equall, R.W., et al., Ultraslow Optical Dephasing in Eu^{3+}: $Y_2 SiO_5$, Physical Review Letters, 72(14) (1994) 2179.
71. Böttger, T., et al., Material Optimization of Er^{3+}: $Y_2 SiO_5$ at 1.5 μm for Optical Processing, Memory, and Laser Frequency Stabilization Applications, in Advanced Optical Data Storage, International Society for Optics and Photonics (2003).
72. Böttger, T., et al., Effects of Magnetic Field Orientation on Optical Decoherence in Er^{3+}: $Y_2 SiO_5$, Physical Review B, 79(11) (2009) 115104.
73. Boukerika, A., et al., Ce-doped YAG Phosphors Prepared via sol-gel Method: Effect of Some Modular Parameters, Journal of Alloys and Compounds, 614 (2014) 383-388.

74. Shi, P., et al., Study on the Five Dynasty Sky-Green Glaze From Yaozhou Kiln and its Coloring Mechanism, Ceramics International, 43(3) (2017) 2943-2949.
75. Hora, D.A., et al., X-ray Excited Optical Luminescence of Eu-doped YAG Nanophosphors Produced via Glucose Sol-Gel Route. Ceramics International, 42(8) (2016) 10516-10519.
76. Grigorjevaite, J. et al., Luminescence and Luminescence Quenching of $K_2Bi(PO_4)(MoO_4):Eu^{3+}$ Phosphors with Efficiencies Close to Unity, ACS Applied Materials & Interfaces, 8(46) (2016) 31772-31782.
77. Yamaji, A., et al., Scintillation Properties of Er-doped $Y_3Al_5O_{12}$ Single Crystals, Radiation Measurements, 56 (2013) 116-119.
78. Zorenko, Y., et al., Luminescent Properties and Energy Transfer Processes in YAG:Er Single Crystalline Films, Journal of Luminescence, 154 (2014) 198-203.
79. Aguilar-Elguézabal, A., et al., Synthesis of $CoAl_2O_4/Al_2O_3$ Nanoparticles For Ceramic Blue Pigments, Ceramics International, 43(17) (2017) 15254-15257.
80. Emiliani, E., et al., Thulium Laser for the Treatment of Upper Urinary Tract Carcinoma (UTUC)? Are We There, Yet? World Journal of Urology, 33(4) (2015) 595-597.
81. Diaz-Torres, L. A., et al., Enhanced Cooperative Absorption and Upconversion in Yb^{3+} Doped YAG Nanophosphors, Optical Materials, 27(7) (2005) 1305-1310.
82. Zhydachevskii, Y., et al., Crystal Structure and Luminescent Properties of Nanocrystalline YAG and YAG:Nd Synthesized By Sol-Gel Method, Optical Materials, 34(12) (2012) 1984-1989.
83. Benayas, A., et al., Nd:YAG Near-Infrared Luminescent Nanothermometers, Advanced Optical Materials, 3(5) (2015) 687-694.
84. Wolters, M., et al., Tm:YAG Laser En Bloc Mucosectomy for Accurate Staging of Primary Bladder Cancer: Early Experience, World Journal of Urology, 29(4) (2011) 429-432.
85. Skaudzius, R., et al., Luminescence Properties of Ln^{3+} -doped (Ce^{3+}, Eu^{3+}, Tb^{3+} or Er^{3+}) Mixed-Metals $Y_3(Al,In)_5O_{12}$ and $Y_3Al_{4.75}Cr_{0.25}O_{12}$ garnets synthesized by Sol-Gel Method, Materials Chemistry and Physics, 170 (2016) 229-238.
86. Praveena, R., et al., Luminescence Properties of $Lu_3Al_5O_{12}:Tb^{3+}$ Nano-Garnet, Journal of the Korean Physical Society, 64(12) (2014) 1859-1865.
87. Upasani, M., Synthesis of $Y_3Al_5O_{12}$:Tb & $Y_3Al_5O_{12}$:Tb,Si Phosphor by Combustion Synthesis: Comparative Investigations on the Structural and Spectral Properties, Optical Materials, 64 (2017) 70-74.
88. Wang, J. Y., et al., Synthesis and Characterization of Fine-Particle $Y_3Al_5O_{12}$: Tb Phosphor By Combustion Process, Journal of Inorganic Materials, 18(1) (2003) 246-250.

89. Shionoya, S., W.M. Yen, and H. Yamamoto, Phosphor handbook, CRC press, (2006).
90. Kang, Y., et al., Preparation of Non-Aggregation YAG-Ce Phosphor Particles by Spray Pyrolysis, Journal of Aerosol Science, 29 (1998) S911-S912.
91. Zhou, Y., et al., Synthesis-Dependent Luminescence Properties of $Y_3Al_5O_{12}$: Re^{3+} (Re= Ce, Sm, Tb) Phosphors, Materials Letters, 56(5) (2002) 628-636.
92. Kiss, Z., et al., Cross-Pumped Cr^{3+}− Nd^{3+}: YAG Laser System, Applied Physics Letters, 5(10) (1964) 200-202.
93. Fujioka, K., et al., Luminescence Properties of Highly Cr Co-Doped Nd:YAG Powder Produced by Sol-Gel Method, Journal of Luminescence, 130(3) (2010) 455-459.
94. Raudonyte, E., et al., On the Ce^{3+} -> Cr^{3+} Energy Transfer in $Lu_3Al_5O_{12}$ Garnets, Optical Materials, 37 (2014) 204-210.
95. Kvapil, J., et al., Laser Properties of YAG: Nd, Cr, Ce. Czechoslovak Journal of Physics B, 34(6) (1984) 581-588.
96. Yagi, H., et al., The Optical Properties and Laser Characteristics of Cr^{3+} and Nd^{3+} Co-Doped $Y_3Al_5O_{12}$ Ceramics, Optics & Laser Technology, 39(6) (2007) 1295-1300.
97. Pruss, D., et al., Efficient Cr^{3+} Sensitized Nd^{3+}: GdScGa-Garnet Laser at 1.06 μm, Applied Physics B, 28(4) (1982) 355-358.
104. Ueda, J., et al., Bright Persistent Ceramic Phosphors of Ce^{3+}-Cr^{3+}-Codoped Garnet Able to Store by Blue Light, Applied Physics Letters, 104(10) (2014) 101904.
99. Dieke, G. H., et al., The Spectra of the Doubly and Triply Ionized Rare Earths, Applied optics, 2(7) (1963) 675-686.
100. Chen, L., et al., The Effect of Electron Cloud Expansion on the Red Luminescence of $Sr_4Al_{14}O_{25}$: Mn^{4+} Revealed by Calculation of the Racah Parameters, Journal of Alloys and Compounds, 613 (2014) 312-316.
101. Murasik, A., et al., Crystal Field Splitting, Institute of Atomic Energy, 30 (1999) 68.
102. Singha, D.K., et al., Visible Detection of Explosive Nitroaromatics Facilitated by a Large Stokes Shift of Luminescence Using Europium and Terbium Doped Yttrium Based MOFs, RSC Advances, 5(123) (2015) 102076-102084.
103. Shaheen, S.E., et al., 2.5% Efficient Organic Plastic Solar Cells, Applied Physics Letters, 78(6) (2001) 841-843.
104. Träger, F., Springer Handbook of Lasers and Optics, Springer Science & Business Media, (2012).
105. Panjwani, D.R., Metal Blacks As Scattering Centers To Increase The Efficiency Of Thin Film Solar Cells, (2011).

106. Bardeen, C.J., et al., Effect of Pulse Shape on the Efficiency of Multiphoton Process: Implications for Biological Microscopy, Journal of Biomedical Optics, 4(3) (1999) 362-368.
107. Feron, K., et al., Spatially Resolved Photocurrent Measurements of organic Solar Cells: Tracking Water Ingress At Edges And Pinholes, Solar Energy Materials and Solar Cells, 109 (2013) 169-177.
108. Coffey, D. C., et al., Mapping Local Photocurrents in Polymer/Fullerene Solar Cells with Photoconductive Atomic Force Microscopy, Nano letters, 7(3) (2007) 738-744.
109. Delamarre, A., et al., Quantitative Luminescence Mapping of Cu (In, Ga) Se_2 Thin-Film Solar Cells. Progress in Photovoltaics: Research and Applications, 23(10) (2015) 1305-1312.
110. Delamarre, A., Contactless Mapping of Saturation Currents of Solar Cells by Photoluminescence, Applied Physics Letters, 100(13) (2012) 131108.
111. Chang, C.-I., Hyperspectral Imaging: Techniques for Spectral Detection and Classification, Springer Science & Business Media, 1 (2003).
112. G. Blasse et al., Luminescent Materials, Berlin: Springer-Verlag, 233 (1994).
113. Chroma, M., et al., Processing and Characterization of Sol-Gel Fabricated Mixed Metal Aluminates, Ceramics International, 31(8) (2005) 1123-1130.
114. Melnikov, P., et al., Mechanism of Thermal Decomposition of Yttrium Nitrate Hexahydrate, Y(NO3)(3)Center Dot 6H(2)O and Modeling of Intermediate Oxynitrates, Journal of Thermal Analysis and Calorimetry, 111(1) (2013) 115-119.
115. Ogieglo, J. M., et al., Luminescence and Energy Transfer in $Lu_3Al_5O_{12}$ Scintillators Co-Doped with Ce^{3+} and Tb^{3+}. Journal of Physical Chemistry A, 116(33) (2012) 8464-8474.
116. Park, J.Y., et al., Solvothermal Synthesis and Luminescence Properties of Tb^{3+}-Doped Gadolinium Aluminum Garnet, Journal of Luminescence, 130(3) (2010) 478-482.
117. Watras, A., et al., Luminescence Properties and Determination of Optimal Re^{3+} (Sm^{3+}, Tb^{3+} And Dy^{3+} Doping Levels in the KYP_2O_7 Host Lattice Obtained by Combustion Synthesis, New Journal of Chemistry, 38(10) (2014) 5058-5068.
118. Li, Y.Y., et al., Manipulation of Linearly Polarized States in A Diode-Pumped YAG/Tm:YAG/YAG Bulk Laser, Optics Letters, 39(7) (2014) 1945-1948.
119. Baur, F., et al., Photoluminescence and Energy Transfer Rates and Efficiencies in Eu^{3+} Activated $Tb_2Mo_3O_{12}$, Journal of Materials Chemistry C, 3(9) (2015) 2054-2064.

120. Saiki, T., et al., Cross-Relaxation and Spectral Broadening of Gain for Nd/Cr:YAG Ceramic Lasers with White-Light Pump Source Under High-Temperature Operation, Optics Communications, 284(12) (2011) 2980-2984.
121. Skruodiene, M., et al., Doping Effect of Tb^{3+} Ions on Luminescence Properties of $Y_3Al_5O_{12}$: Cr^{3+} Phosphor, Journal of Luminescence, 179 (2016) 355-360.
122. Guo, X.Y., et al., High-Beam-Quality, Efficient Operation of Passively Q-Switched Yb: YAG/Cr: YAG Laser Pumped by Photonic-Crystal Surface-Emitting Laser, Applied Physics B-Lasers and Optics, 123(7) (2017) 194.
123. Kinsman, K. M., et al. Phase Development and Luminescence in Chromium-Doped Yttrium-Aluminum-Garnet (YAG-Cr) Phosphors, Journal of the American Ceramic Society, 77(11) (1994) 2866-2872.

LIST OF PUBLICATIONS

Articles in journals

1. M. Skruodiene, A. Katelnikovas, L. Vasylechko, R. Skaudzius. Tb^{3+} to Cr^{3+} Energy Transfer in Co-Doped $Y_3Al_5O_{12}$ Host. *Journal of Luminescence*, 208 (2019) 327-333.
2. M. Skruodiene, M. Misevicius, M. Sakalauskaite, A. Katelnikovas, R. Skaudzius. Doping Effect of Tb^{3+} Ions on Luminescence Properties of $Y_3Al_5O_{12}:Cr^{3+}$ Phosphor. *Journal of Luminescence*, 179 (2016) 355-360.

Published contribution to academic conferences

1. M. Skruodiene, R. Skaudzius. Tb^{3+} to Cr^{3+} Energy Transfer and External Quantum Efficiency in co-doped Yttrium Aluminum Garnet Host. 20th International Conference-School "Advanced Materials and Technologies. 2018". 27 – 31 August 2018, Palanga, Lithuania.
2. M. Skruodiene, R. Skaudzius. Tb^{3+} to Cr^{3+} Energy Transfer and External Quantum Efficiency in co-doped Yttrium Aluminum Garnet Host. 2nd NFFA-Europe Summer School Nanoscience Foundries and Fine Analysis (NFFA), available instruments and techniques. 9 – 13 July 2018, Trieste, Italy.
3. M. Skruodiene, R. Skaudzius. Tb^{3+} to Cr^{3+} Energy Transfer in co-doped $Y_3Al_5O_{12}$ (YAG) host. Open readings 2018: 61st International Conference for Students of Physics and Natural Sciences, 20-23 March 2018, Vilnius, Lithuania.
4. M. Skruodiene, R. Skaudzius. Cr^{3+} and Tb^{3+} Co-doped YAG: Promising Phosphors for Solid-State Lighting. Advanced Materials World Congress. 4 – 8 February 2018, Singapore, Singapore.
5. M. Skruodiene, A. Katelnikovas, R. Skaudzius. Cr^{3+} and Tb^{3+} Co-doped YAG: Promising Phosphors for Solid-State Lighting. „There is no Future without the Past": science on the interface of XIX-XXI centuries. The International Conference Dedicated to the 215-th Birth Anniversary of Ignacy Domeyko. 27 – 29 July 2017, Vilnius, Lithuania.
6. M. Skruodiene, A. Katelnikovas, R. Skaudzius. Cr^{3+} and Tb^{3+} Co-doped YAG: Promising Phosphors for Solid-State Lighting. "Nanotechnology and innovation in the Baltic Sea region", NIBS Conference 2017. 14 – 16 June 2017, Kaunas, Lithuania.

7. M. Skruodiene, A. Katelnikovas, R. Skaudzius. Cr^{3+} and Tb^{3+} Co-doped YAG: Promising Phosphors for Solid-State Lighting. International Conference Chemistry and chemical technology 2017. 28th April 2017, Kaunas, Lithuania.
8. M. Skruodiene, M. Misevicius, M. Sakalauskaite, A. Katelnikovas, R. Skaudzius. Doping Effect of Tb^{3+} on Luminescence Properties of $Y_3Al_5O_{12}:Cr^{3+}$ Phosphor. International Conference EcoBalt 2016. 9 – 12 October 2016, Tartu, Estonia.
9. M. Skruodiene, M. Misevicius, M. Sakalauskaite, A. Katelnikovas, R. Skaudzius. Doping Effect of Tb^{3+} Ions on Luminescence Properties of $Y_3Al_5O_{12}:Cr^{3+}$ Phosphor. Chemistry and Chemical Technology: International Conference of Lithuanian Society of Chemistry: Lithuanian Academy of Science. 28 – 29 April 2016, Vilnius, Lithuania.
10. M. Skruodiene, M. Misevicius, M. Sakalauskaite, A. Katelnikovas, R. Skaudzius. Doping Effect of Cr^{3+} Ions Concentration on Luminescence Properties of $Y_3Al_5O_{12}:Cr^{3+},Tb^{3+}$ Phosphor. HINT workshop. Nanostructured materials: protective and functional coatings, surface treatment, bioceramics biocomposites and membranes. 14 – 16 March 2016, Vilnius, Lithuania.
11. M. Skruodiene, M. Misevicius, M. Sakalauskaite, A. Katelnikovas, R. Skaudzius. Doping Effect of Tb on Luminescence Properties of $Y_3Al_5O_{12}$:Cr Phosphor. 2^{nd} International Conference of Chemists Nanochemistry and nanomaterials 2015. 22 – 24 October 2015, Vilnius, Lithuania.
12. M. Skruodiene, M. Misevicius, A. Katelnikovas, R. Skaudzius. Luminescence Properties of YAG:Tb, YAG:Cr and YAG:Tb,Cr Synthesized by Sol-Gel Method. Chemistry and Chemical Technology 2015 : International Conference of Lithuanian Chemical Society, Dedicated to Professor Vitas Dauksas on his 80^{th} Birth Anniversary, 23 January 2015, Vilnius, Lithuania.

NOTES

Vilniaus universiteto leidykla

Universiteto g. 1, LT-01513 Vilnius

El. p. info@leidykla.vu.lt,

www.leidykla.vu.lt

Tiražas 16 egz.